A multiscale thermo-fluid computational model for a two-phase cooling system

Riccardo Sacco[a,*], Lucia Carichino[b], Carlo de Falco[d,e], Maurizio Verri[a], Francesco Agostini[c], Thomas Gradinger[c]

[a] *Dipartimento di Matematica, Politecnico di Milano, Piazza L. da Vinci 32, 20133 Milano, Italy*
[b] *IUPUI Department of Mathematical Sciences, 402 N. Blackford St., LD 270 E Indianapolis, IN 46202-3267, United States*
[c] *ABB Switzerland Ltd., Corporate Research, Segelhofstrasse 1K 5405, Baden-Dättwil, Switzerland*
[d] *MOX Modeling and Scientific Computing, Dipartimento di Matematica, Politecnico di Milano, Piazza L. da Vinci 32, 20133 Milano, Italy*
[e] *CEN Centro Europeo di Nanomedicina, Piazza L. da Vinci 32, 20133 Milano, Italy*

Received 4 April 2014; received in revised form 10 July 2014; accepted 10 August 2014
Available online 22 August 2014

* Corresponding author. Tel.: +39 02 2399 4540; fax: +39 02 2399 4513.
E-mail address: riccardo.sacco@polimi.it (R. Sacco).
URL: http://www1.mate.polimi.it/~ricsac/ (R. Sacco).

1. Introduction and motivation

Ever since the early 1980s the increasing growth of new technologies and applications has been shifting scientific interest on power electronics. In such wide-range industrial context, the necessity to develop devices with a high power dissipation per unit volume has justified the need of advanced cooling systems capable to prevent excessive temperature increase and consequent device failure. Conventional cooling procedures exploit convection heat transfer between a fluid in motion and a bounding surface at different temperatures. Typical examples are water-cooled and air-cooled systems, widely used in power electronics applications. A different approach to cooling is represented by the two-phase thermosiphon device whose functioning principle is schematically illustrated in Fig. 1 and whose structure is shown in Fig. 2(a).

This kind of device consists of an evaporator, attached to the device requiring cooling, and a condenser made up of a stack of fins among which air is allowed to flow. The evaporator and the condenser are connected by a pipe in which a mixture of liquid and vapor phases is flowing. The heat generated by an electronic device in contact with the evaporator is collected by means of an evaporating fluid. The vapor phase fluid, rising in the pipe, passes through the condenser where it returns to the liquid phase. As no pumps are needed to move the refrigerant fluid from the evaporator to the condenser, the resulting thermodynamical efficiency of two-phase cooling systems is remarkably superior to that of water-cooled or air-cooled systems (see [3]). In order to deepen our understanding of the mechanisms that determine the performance of a two-phase thermosiphon cooler device and to facilitate the further optimization of its design, in the present research we focus on the study of the condenser subsystem (see Fig. 2(b)), for which we develop a multiscale mathematical model that is implemented in a numerical simulation code. As computational efficiency is a stringent requirement in industrial design and optimization procedures, model complexity is suitably reduced through the adoption of physically sound consistent assumptions that allow us to end up with a system of nonlinearly coupled 2D PDEs for the air and panel temperatures, and 1D equations within the network of pipes distributed in each fin for the refrigerant fluid flow.

Another important constraint is represented by the ability of the computational method to reproduce on the discrete level important physical features characterizing the problem at hand, such as mass and flux conservation, and its robustness in the presence of dominating convective flow regimes. These requirements are here satisfied by the introduction of a stabilized mixed finite element scheme on quadrilateral grids that automatically provides the desired inter-element flux conservation and upwinding through the use of suitable quadrature rules for the mass flux matrix and convection term. The resulting discrete method has also an immediate interpretation in terms of finite volume formulation which allows a compact implementation of the scheme that highly improves the overall efficiency of the computer-aided design procedure.

A final issue of critical importance in the development of a reliable computational tool for use in industrial design is model calibration and validation. Model calibration is properly addressed by supplying the parameter setting in the equation system with suitable *empirical correlations*, that are functional relations between two or more physical variables, usually obtained by means of a series of experimental tests. In common engineering practice, correlations are widely used because they allow to account for complex physical phenomena in a simple and synthetic manner, albeit their applicability is clearly restricted to a specific admissible range of parameter values. Model validation is carried out through extensive numerical simulations of the two-phase condenser under realistic working conditions.

An outline of the article is as follows. Section 2.1 describes the two-dimensional model for heat convection in air and heat diffusion in the panel whose derivation from the corresponding full 3D model is outlined in the Appendix. The simplified geometrical representation of the coolant-filled channel and the system of 1D equations describing the flow within it are dealt with in Section 2.2. Section 3 discusses the decoupled iterative algorithm used to solve the complete model while Sections 4 and 5 are devoted to the discussion of the discretization techniques adopted to treat each differential subsystems arising from system linearization. Finally, in Section 6 simulation results are presented and discussed and in Section 7 conclusions are drawn and possible future research directions are addressed.

2. Mathematical models

In this section we describe the mathematical model on which our numerical simulation tool for the condenser is based. The equations for heat convection in air and heat diffusion in the panel wall are presented in Section 2.1, while the model for the two-phase flow in the channel is in Section 2.2.

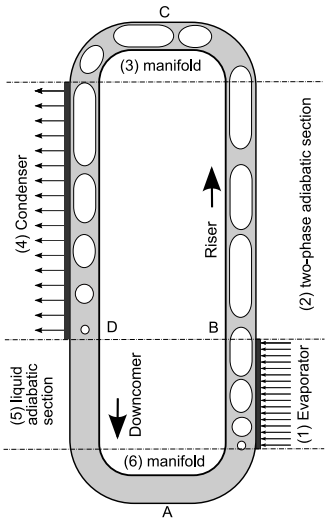

Fig. 1. Schematic representation of the working principle of a thermosiphon cooler.

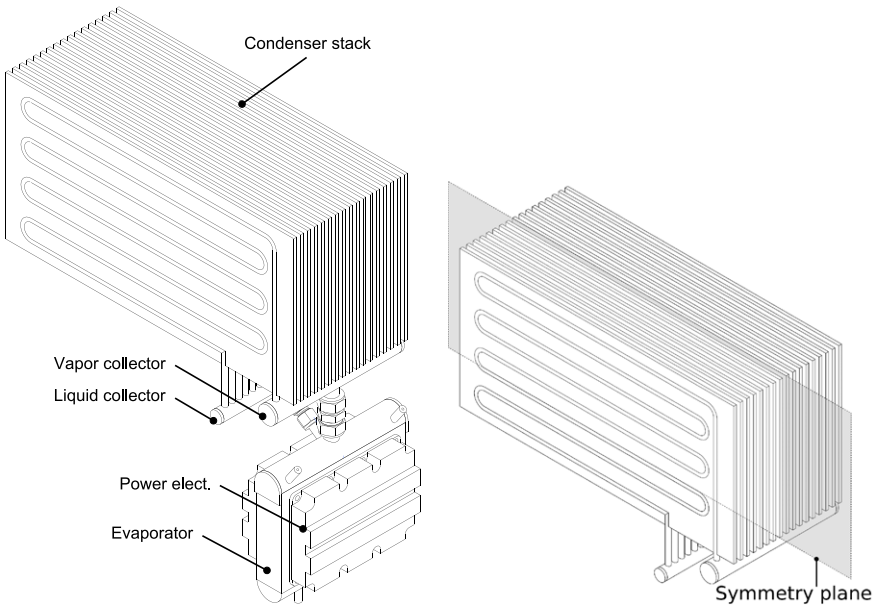

(a) Cooling system assembly.

(b) Details of the condenser and symmetry plane.

Fig. 2. Two-phase cooling system based on the thermosiphon principle [1,2].

2.1. 2D model for the panel wall and air flow

The model for heat diffusion and convection is based on the following set of simplifying assumptions:

(H1) the geometry of the channel embedded into each panel of the condenser is the same;
(H2) air flow is in steady-state conditions;
(H3) air flow conditions in between each pair of condenser fins are identical;
(H4) air flow velocity $\boldsymbol{v}_a$ is everywhere parallel to the fin plates and its magnitude varies only in the orthogonal direction;
(H5) air density ρ_a is constant;

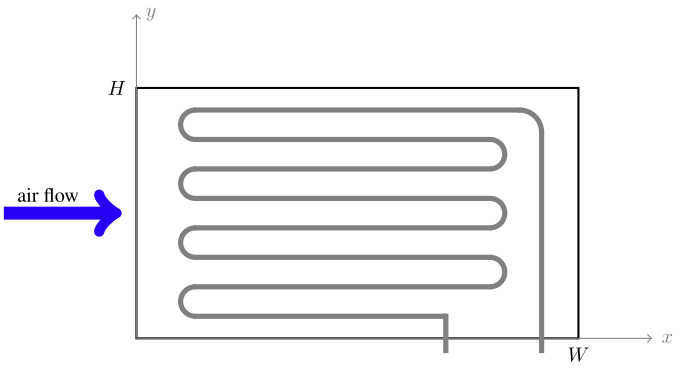

Fig. 3. Computational domain for the two-dimensional heat flow problem.

(H6) the thickness of each panel is negligible compared to its size in any other direction;
(H7) the thickness of the air layer separating two panels in the condenser is negligible compared to the panel size in any other direction.

Under the assumptions above, symmetry considerations lead to define the simplified computational domain $\Omega := (0, W) \times (0, H) \subset \mathbb{R}^2$ illustrated in Fig. 3 and corresponding to a cut of the 3D geometry along the symmetry plane represented in Fig. 2(b), in such a way that the air temperature T_a and panel temperature T_w satisfy in Ω the following equations which express conservation of energy:

$$\boldsymbol{\nabla} \cdot (-k_a \boldsymbol{\nabla} T_a + \rho_a c_p \widetilde{\boldsymbol{v}}_a T_a) + \widetilde{h}_{aw}(T_a - T_w) = 0, \tag{1a}$$

$$\boldsymbol{\nabla} \cdot (-k_w \boldsymbol{\nabla} T_w) + h^*_{aw}(T_w - T_a) + h^*_{wc}(T_w - T_c) = 0, \tag{1b}$$

complemented by the boundary conditions:

$$T_a = T_a{}^{\text{in}} \quad y = 0, \tag{1c}$$

$$-k_a \boldsymbol{\nabla} T_a \cdot \boldsymbol{n} = 0 \quad y = H, \tag{1d}$$

$$(-k_a \boldsymbol{\nabla} T_a + \rho_a c_p \widetilde{\boldsymbol{v}}_a T_a) \cdot \boldsymbol{n} = 0 \quad x = 0,\ x = W, \tag{1e}$$

$$-k_w \boldsymbol{\nabla} T_w \cdot \boldsymbol{n} = 0 \quad y = 0,\ y = H,\ x = 0,\ x = W. \tag{1f}$$

The unknown functions $T_a = T_a(x, y)$ and $T_w = T_w(x, y)$ are the air and wall temperature respectively, c_p is the air specific heat capacity at constant pressure and k_a and k_w are the thermal conductivities of air and panel material (*e.g.*, aluminum), respectively. The function $T_c = T_c(x, y)$ represents the temperature of the cooling two-phase fluid in the channel network and is assumed to be a given datum in the solution of the equation system (1). The parameters $\widetilde{h}_{aw}$ and h^*_{aw} are the heat transfer coefficient h_{aw} between air and condenser wall divided by suitably defined characteristic lengths λ_{1a} and λ_{1w}, respectively. Precisely, λ_{1a} is related to the variation of k_a in the direction between air and condenser wall while λ_{1w} is related to the variation of k_w in the thickness of the condenser wall. The quantity h^*_{wc} is the heat exchange coefficient h_{wc} between the fluid and the panel wall divided by λ_{1w}. The vector field $\widetilde{\boldsymbol{v}}_a$ is the air flow velocity $\boldsymbol{v}_a$ multiplied by the factor $\lambda_{2a}/\lambda_{1a}$ where λ_{2a} is another characteristic length related to the formation of the thermal boundary layer at the interface between air and panel. The quantities W and H are the size of the panel in the x and y directions, respectively, and $\boldsymbol{n}$ is the outward unit vector along the external surface of Ω. It is important to notice that the physical properties of air, namely k_a and c_p, as well as the panel material properties, *e.g.* k_w, and, when simulations are carried out in the natural convection regime, also the magnitude of the air velocity $\widetilde{\boldsymbol{v}}_a$, depend on the temperatures T_a and T_w, hence problem (1) is nonlinear. In particular, in the case of natural convection, $\widetilde{\boldsymbol{v}}_a$ depends on the average air temperature $\langle T_a \rangle$ and on T_a^{in} through the following expression derived from [4]

$$\widetilde{\boldsymbol{v}}_a = \frac{\rho_a\ g\ S^2\ \beta\ (\langle T_a \rangle - T_a^{\text{in}})}{12\ \mu_a}$$

where g is the magnitude of the gravitational acceleration, β is the air expansion coefficient, S is the distance between two panels and μ_a is the air dynamic viscosity. The heat exchange coefficient h_{aw}, and therefore $\widetilde{h}_{aw}$ and h^*_{aw}, are

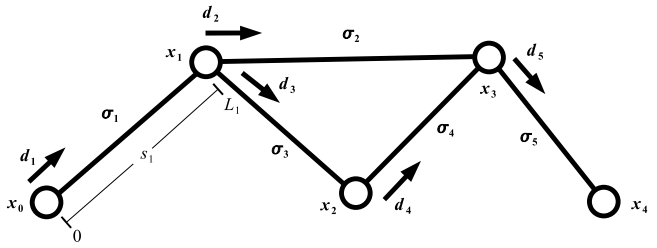

Fig. 4. Example of channel network geometry and notation.

also allowed to depend on the air temperature and velocity, in particular through the correlations given in [4] in the natural convection regime and through the Chilton–Colburn correlation for the forced convection regime (see, *e.g.*, [5, p. 395]). The detailed derivation of (1) from the corresponding 3D model is illustrated for convenience in the Appendix.

2.2. Model for the channel subsystem

The model for the two-phase flow in the pipes embedded in the condenser is based on the following set of simplifying assumptions:

(H8) the two-phase flow in the pipeline is in steady-state conditions;
(H9) the flow velocity is axially directed along the pipeline;
(H10) the liquid and vapor phases move with the same velocity and are in thermal equilibrium with each other over each cross-sectional area of the flow;
(H11) the two-phase flow properties are uniform over each cross-sectional area;
(H12) the specific kinetic and potential energies of the fluid are negligible with respect to its specific enthalpy;
(H13) the cross-sectional area of the pipe in the direction orthogonal to fluid flow is the same everywhere;
(H14) the pipe geometry may include any number of bifurcations, but there are only one *inlet* and one *outlet* pipe connecting the condenser to the evaporator.

Hypotheses (H8)–(H11) comprise the basis for the application of the so called *homogeneous flow model* for analyzing one-dimensional multiphase flows. In such a model the two-phase flow is treated as a single-phase flow having average fluid properties, which depend upon temperature and mixture quality (see, *e.g.*, [6, Chapter 9], or [7, Chapter 3]). Although the liquid and vapor phases are not always traveling at the same velocity, the assumption of having a homogeneous flow is a common practice in many engineering applications, and provides a solid first approximation of the void fraction prediction limiting the complexity of the model. As an example, many bubbly or mist flows, where the difference in velocity between the entrained phase and the continuous phase is almost negligible can, to a first approximation, be considered to be homogeneous.

Assumption (H12) is reasonable for the pipe dimensions and flow mass and velocities we are interested in and is often made in other models for cooling devices working in the same conditions (*e.g.*, [8]).

Assumptions (H13) and (H14) about the geometry of the pipeline are taken mainly for the sake of presentation clarity as they greatly simplify the notation of the flow equations and boundary/coupling conditions, but the modifications required to relax those assumptions are actually quite straightforward. Before we describe the model equations for the two-phase coolant flow, the introduction of some notation for the flow domain geometry is in order.

The channel embedded in each panel, where the two-phase coolant flows, is modeled as a pipeline network [9–12], *i.e.*, a set of a number M of 1D straight pipe segments $\boldsymbol{\sigma}_j \subset \Omega,\ j = 1, \ldots, M$. Such segments are joined at a set of N vertices $\mathbf{x}_i \in \Omega,\ i = 1, \ldots, N$ and each is parametrized by a (scalar) local coordinate s_j such that $0 \le s_j \le L_j$, L_j being the length of $\boldsymbol{\sigma}_j$ (see Fig. 4).

For each junction $\mathbf{x}_i$, we denote by $I_i^- \subseteq \{1, \ldots, N\}$, the set of those indices j for which $\mathbf{x}_i$ is the *first endpoint* of the segment $\boldsymbol{\sigma}_j$, *i.e.*, $j \in I_i^- \Leftrightarrow \mathbf{x}(s_j)|_{s_j=0} = \mathbf{x}_i$, where $\mathbf{x}$ is the (vector) Cartesian coordinate. Similarly, we define $I_i^+ \subseteq \{1, \ldots, N\}$, to be the set of those indices j for which $\mathbf{x}_i$ is the *second endpoint* of the segment $\boldsymbol{\sigma}_j$, *i.e.*, $j \in I_i^+ \Leftrightarrow \mathbf{x}(s_j)|_{s_j=L_j} = \mathbf{x}_i$. We assume each parametrization to be *uniform*, *i.e.*, $j \in I_m^- \cap I_n^+ \Leftrightarrow \mathbf{x}(s_j) = \mathbf{x}_m + \mathbf{d}_j s_j$, where $\mathbf{d}_j = (\mathbf{x}_n - \mathbf{x}_m)/L_j$ is the unit vector defining the *direction* of $\boldsymbol{\sigma}_j$. Furthermore, we introduce the two additional

vertices $\mathbf{x}_0$ and $\mathbf{x}_{N+1}$ representing the *inlet* and the *outlet* of the channel and we assume that they are connected to the first node of the first pipe and second node of the last pipe, respectively, so that we have $I_0^- \equiv \{1\}$, $I_0^+ \equiv \varnothing$, $I_{N+1}^- \equiv \varnothing$ and $I_{N+1}^+ \equiv \{M\}$. Finally, we denote by $|\Sigma_j|$ the cross-sectional area of each network segment and, according to (H13), we assume $|\Sigma_j| = |\Sigma|,\ j \in 1, \dots, M$.

Using the notation defined above and the assumptions (H8)–(H13), the conservation of mass, momentum and energy within each pipe $\boldsymbol{\sigma}_j$ may be expressed by the following system of 1D equations:

$$\partial_{s_j} G_j = 0, \tag{2a}$$

$$\partial_{s_j} \frac{G_j^2}{\rho_j} = -\partial_{s_j} p_j + f_j + \rho_j \mathbf{g} \cdot \mathbf{d}_j, \tag{2b}$$

$$\partial_{s_j} \left(G_j \mathcal{H}_j \right) = h_{wc} \left(T_w - T_{c,j} \right). \tag{2c}$$

The quantities G_j, ρ_j, p_j, f_j, $\mathcal{H}_j$ and $T_{c,j}$ are momentum, density, pressure, frictional forces, specific enthalpy and temperature of the two-phase fluid in each segment $\boldsymbol{\sigma}_j$, respectively, while $\mathbf{g}$ is the vector denoting the gravitational acceleration. A fully detailed derivation of system (2) is given, *e.g.*, in [7, Chapter 3]. System (2) is the (stationary) extension to the case of a pipeline network with bifurcations of the model for the simulation of cooling devices proposed and numerically investigated in [8].

In view of numerical discretization, it is convenient to rewrite Eqs. (2a)–(2b) as:

$$\begin{cases} \partial_{s_j} G_j = 0 \\ \partial_{s_j} \varphi_j = R_j G_j + \rho_j \mathbf{g} \cdot \mathbf{d}_j \end{cases} \tag{3}$$

where $\varphi_j = G_j^2/\rho_j + p_j$ denotes the total dynamical pressure and $R_j = f_j/G_j$ denotes the pipe hydraulic resistance per unit length. Similarly, Eq. (2c), upon introducing the symbol $\mathcal{W}_j$ denoting the enthalpy flux, can be rewritten as:

$$\begin{cases} \partial_{s_j} \mathcal{W}_j = h_{wc}(T_w - T_{c,j}) \\ \mathcal{W}_j = G_j \mathcal{H}_j. \end{cases} \tag{4}$$

To close system (2), we need:

1. a set of *coupling* conditions at the N junctions $\mathbf{x}_i,\ i = 1, \dots, N$;
2. a set of *boundary* conditions at the inlet and outlet sections;
3. a set of *constitutive relations*.

All of these relations will be defined in the subsections below.

2.2.1. Coupling conditions

At each of the junction nodes $\mathbf{x}_i$ we impose the following *coupling conditions*, $\forall i \in \{1, \dots, N\}$, $\forall j \in I_i^-$, $\forall k \in I_i^+$:

$$\varphi_j|_{s_j=0} = \varphi_k|_{s_k=Lk}, \tag{5a}$$

$$\mathcal{H}_j|_{s_j=0} = \mathcal{H}_k|_{s_k=Lk}, \tag{5b}$$

$$\sum_j -G_j|_{s_j=0} + \sum_k G_k|_{s_k=Lk} = 0, \tag{5c}$$

$$\sum_j -\mathcal{W}_j|_{s_j=0} + \sum_k \mathcal{W}_k|_{s_k=Lk} = 0. \tag{5d}$$

These conditions express continuity of total dynamical pressure and enthalpy and conservation of mass and enthalpy fluxes at the junctions.

2.2.2. Boundary conditions

At the inlet $\mathbf{x}_0$ and outlet $\mathbf{x}_{N+1}$ we apply the following boundary conditions:

$$\varphi_1|_{s_1=0} = p_{\text{inlet}}, \tag{6a}$$

$$\mathcal{H}_1|_{s_1=0} = \mathcal{H}_{\text{inlet}}, \tag{6b}$$
$$G_1|_{s_1=0} = G_M|_{s_M=L_M} = G_{\text{tot}}, \tag{6c}$$

where p_{inlet}, $\mathcal{H}_{\text{inlet}}$ and G_{tot} are given data.

2.2.3. Constitutive relations

In order to introduce the constitutive relations for the homogeneous two-phase fluid, let us denote by

$$dV_j(s_j) = |\Sigma|\, ds_j$$

the infinitesimal volume of a trait of the pipeline segment $\boldsymbol{\sigma}_j$ contained between the cross-sections of curvilinear coordinates s_j and $s_j + ds_j$. Let $dV_{V,j}(s_j)$ and $dV_{L,j}(s_j)$ denote the part of such volume occupied by the vapor and liquid phase respectively. As a consequence of assumptions (H10)–(H11), the fluid vapor mixture contained in dV_j may be assumed to be in saturation, therefore the densities and enthalpies over the flow cross-section at s_j of each phase, as well as the mixture pressure, may be expressed as functions of temperature, *i.e.*:

$$\begin{aligned}
&\rho_{V,j} = \rho_V(T_{c,j})\\
&\rho_{L,j} = \rho_L(T_{c,j})\\
&\mathcal{H}_{V,j} = \mathcal{H}_V(T_{c,j})\\
&\mathcal{H}_{L,j} = \mathcal{H}_L(T_{c,j})\\
&\mu_{V,j} = \mu_{V,j}(T_{c,j})\\
&\mu_{L,j} = \mu_{L,j}(T_{c,j})\\
&h_{wc,V} = h_{wc,V}(T_{c,j})\\
&h_{wc,L} = h_{wc,L}(T_{c,j})\\
&p_j = p(T_{c,j}).
\end{aligned} \tag{7a}$$

Standard reference correlations expressing the temperature dependencies of the properties listed in (7a) are given in the literature for relevant coolant fluids. We use in particular those presented in [13] for the R245fa fluid and those of [14] for R134a, as computed via the National Institute of Standards and Technology standard reference data program REFPROP [15]. We define the *vapor quality* $x_j := x\ (s_j)$ as the ratio

$$x_j := \frac{\rho_{V,j}\, dV_{V,j}}{\rho_{V,j}\, dV_{V,j} + \rho_{L,j}\, dV_{L,j}}. \tag{7b}$$

The two-phase density may be defined as

$$\rho_j := \frac{\rho_{V,j}\, dV_{V,j} + \rho_{L,j}\, dV_{L,j}}{dV_{V,j} + dV_{L,j}}. \tag{7c}$$

Using (7b) and (7c) one easily gets

$$\rho_j = \frac{\rho_V(T_{c,j})\rho_L(T_{c,j})}{(1-x_j)\rho_V(T_{c,j}) + x_j\rho_L(T_{c,j})}, \tag{7d}$$

which relates the two-phase density to the temperature and void fraction. Similarly the two-phase specific enthalpy is given by

$$\mathcal{H}_j = (1-x_j)\mathcal{H}_L(T_{c,j}) + x_j\mathcal{H}_V(T_{c,j}), \tag{7e}$$

while the two-phase dynamic viscosity is

$$\mu_j = x_j\mu_V + (1-x_j)\mu_L.$$

All the single-phase quantities depend implicitly on the temperature $T_{c,j}$ of the two-phase fluid in the jth segment $\boldsymbol{\sigma}_j$, hence system (7) is nonlinear.

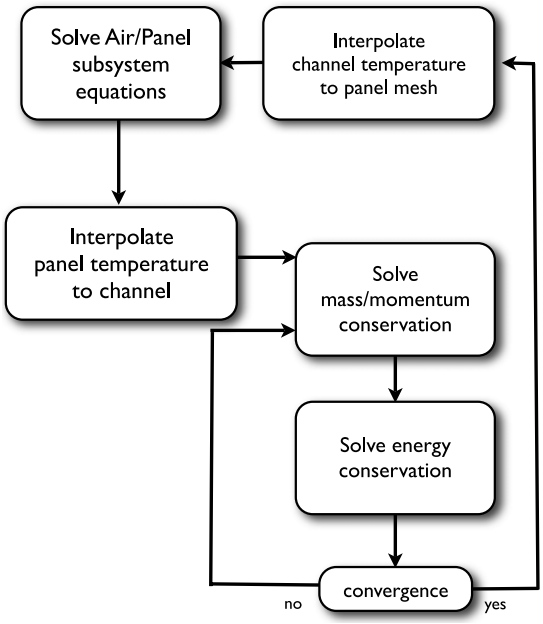

Fig. 5. Schematic representation of the staggered iteration algorithm.

After analyzing the review of the most recent correlation of the heat transfer coefficient h_{wc} for condensation inside tubes [16,17], we have decided to consider the *Shah* correlation [18], valid for film condensation pattern, in the following modified version proposed in [19, Chapter 4]

$$h_{wc}|_{\sigma_j} = h_{wc,L}\left[(1-x_j)^{0.8} + \frac{3.8x_j^{0.76}\left(1-x_j\right)^{0.04}}{p_r^{0.38}}\right] + x_j^{\theta} h_{wc,V}$$

where p_r is the reduced pressure, *i.e.* the ratio between the fluid pressure and the pressure at the critical point, $h_{wc,L}$ and $h_{wc,V}$ are the heat transfer coefficients assuming a single phase flowing in the pipe, and θ is a weighting coefficient to modulate the contribution of the vapor phase to the homogenized heat transfer coefficient. To model the frictional forces f_j we used the following relation based on the *Blasius equation* [20, Chapter 13]

$$f_j = \frac{2C_f G_j^2}{\rho_j D}$$

where D is the hydraulic diameter of the pipe, C_f is the frictional coefficient

$$C_f = \frac{0.079}{\mathbb{R}e_j{}^{1/4}},$$

and the Reynolds number $\mathbb{R}e_j$ is

$$\mathbb{R}e_j = \frac{|G_j|D}{\mu_j}.$$

3. Iterative algorithms

The staggered algorithm used for the coupling of the different subsystems is depicted in the flow-chart of Fig. 5.

The procedure consists of a nested fixed-point iteration composed of: (1) an outer iteration loop to solve the 2D air/panel subsystem; and (2) an inner iteration loop to solve the non-linear problems within each subsystem. In more detail, the outer iteration proceeds as follows:

1. Given T_c and $\widetilde{h}_{aw}$, compute a new value for T_a and T_w by solving system (1).
2. Determine the value of T_w at each node of the channel network.
3. Solve system (2) to update the quantities $G, \mathcal{H}, p$ describing the state of the fluid flow in the channel and, as a by-product, compute the fluid temperature T_c and the vapor quality.
4. Go back to step 1.

Inner iteration loops are required to solve the non-linear heat flow equations at step 1 and for solving the nonlinear coupled system for the two phase flow at step 3. For the former we employ a monolithic quasi-Newton algorithm, while for the latter we further decouple the equations and proceed as follows:

3.1. Solve subsystem (2a)–(2b) to update G and p.
3.2. Solve subsystem (2c) to update $\mathcal{H}$.
3.3. Determine the density, temperature and vapor quality using system (7).
3.4. Go back to step 3.1.

4. Dual mixed-finite volume discretization of the 2D subproblems

In this section we describe the dual mixed-finite volume (MFV) method used for the numerical approximation of the air/panel physical model, presented in Section 2.1. The choice of the dual-mixed finite element method is due to the fact that, in its lowest order form, it preserves flux continuity across interelement boundaries with a piecewise constant discontinuous approximation of the scalar unknown that makes it structurally similar to standard finite volume schemes. A sound theoretical foundation (see [21,22] for an introduction and analysis), confirmed by the included computational experiments, is a final motivation for selecting the MFV approach in the discretization of the model system (1).

4.1. Dual mixed finite element approximation

Consistently with Section 2.1, we assume that the computational domain Ω is a rectangular open bounded set of $\mathbb{R}^2$ and denote by $\Gamma := \partial\Omega$ and $\boldsymbol{n}$ the domain boundary and its outward unit normal vector, respectively. Then, we consider the following advection–diffusion–reaction model problem in mixed form:
find $u : \Omega \to \mathbb{R}$ and $\boldsymbol{J} : \Omega \to \mathbb{R}^2$ such that:

$$a\boldsymbol{J} + \nabla u - a\boldsymbol{\beta} u = \boldsymbol{0} \qquad \text{in } \Omega, \tag{8a}$$

$$\nabla \cdot \boldsymbol{J} + \gamma u = f \qquad \text{in } \Omega, \tag{8b}$$

$$u = 0 \qquad \text{on } \Gamma. \tag{8c}$$

In (8a), $a := \alpha^{-1}$ is the inverse diffusion coefficient, α being a strictly positive quantity which for ease of presentation and with no loss of generality is assumed constant in the present section. Furthermore the convective field $\boldsymbol{\beta}$ is a given constant vector, while $f \in L^2(\Omega)$ and $\gamma \in L^\infty(\Omega)$ are given functions, with $\gamma(\boldsymbol{x}) > 0$. We also let $\boldsymbol{J} := -\alpha\nabla u + \boldsymbol{\beta} u$ be the flux associated with u, and we assume that (see [23,24])

$$\frac{\|\boldsymbol{\beta}\|_{L^\infty(\Omega)}}{4\,\alpha\,\inf\limits_{\Omega}(\gamma)} < 1. \tag{9}$$

Eq. (1a) is a special case of (8) upon setting $u := T_a, \alpha := k_a, \boldsymbol{\beta} := \rho_a c_p \widetilde{\boldsymbol{v}}_a, \gamma := \widetilde{h}_{aw}$ and $f := \widetilde{h}_{aw} T_w$, with T_w a known function, while Eq. (1b) is a special case of (8) upon setting $u := T_w, \alpha := k_w, \boldsymbol{\beta} := \boldsymbol{0}, \gamma := h^*_{aw} + h^*_{wc}$ and $f := h^*_{aw} T_a + h^*_{wc} T_c$, with T_a and T_c known functions. Homogeneous Dirichlet boundary conditions for u are assumed only for ease of presentation, because mixed and/or Neumann conditions can be easily handled by the proposed scheme (see [25,26]).

In view of the numerical approximation of (8), we introduce a regular decomposition $\mathcal{T}_h$ of Ω into `Nel` rectangles K of area $|K|$ and center of gravity $\boldsymbol{x}_{G,K}$, and we denote by $\mathcal{E}_h$ the set of edges of $\mathcal{T}_h$ and by `Ned` the number of total edges of the mesh. We also let $\mathcal{E}_h^{\text{in}}$ denote the set of internal edges of $\mathcal{E}_h$. Let $\mathbb{P}_{k_1,k_2}$ be the space of polynomials of degree less than or equal to k_1 with respect to x and less than or equal to k_2 with respect to y. Let $k \geq 0$; for each $K \in \mathcal{T}_h$ we denote by $\mathbb{RT}_{[k]}(K) := \mathbb{P}_{k+1,k}(K) \times \mathbb{P}_{k,k+1}(K)$ the kth order *Raviart–Thomas* (RT) mixed finite element space [27]

and by $\mathbb{Q}_k(K) = \mathbb{P}_{k,k}(K)$. We introduce the functional spaces $\mathbf{V} \equiv H_{\mathrm{div}}(\Omega) = \left\{\boldsymbol{v} : \boldsymbol{v} \in [L^2(\Omega)]^2,\ \nabla \cdot \boldsymbol{v} \in L^2(\Omega)\right\}$ and $\mathbf{Q} \equiv L^2(\Omega)$, and their corresponding finite dimensional approximations:

$$\mathbf{V}_h = \left\{\boldsymbol{v}_h \in \mathbf{V} :\ \boldsymbol{v}_h|_K \in \mathbb{RT}_{[0]}(K)\ \forall K \in \mathcal{T}_h\right\},$$
$$\mathbf{Q}_h = \left\{q_h \in \mathbf{Q} :\ q_h|_K \in \mathbb{Q}_0(K)\ \forall K \in \mathcal{T}_h\right\}.$$

Functions in $\mathbf{V}_h$ are linear along each coordinate direction and discontinuous over $\mathcal{T}_h$ but have continuous normal component across each edge $e \in \mathcal{E}_h^{\mathrm{in}}$. Functions in Q_h are piecewise constant and discontinuous over $\mathcal{T}_h$.

To reflect the different nature of the degrees of freedom of functions in $\mathbf{V}_h$ and $\mathbf{Q}_h$, we introduce two different adjacency structures.

For each (oriented) edge $\boldsymbol{e} \in \mathcal{E}_h^{\mathrm{in}}$, we indicate by $|\boldsymbol{e}|$ the length of $\boldsymbol{e}$, and we denote by K_e^+ and K_e^- the pair of mesh elements such that $\boldsymbol{e} = \partial K_e^+ \cap \partial K_e^-$. We also denote by $\boldsymbol{n}_e^+$ the unit normal vector on $\boldsymbol{e}$ pointing from K_e^+ to K_e^- and define $\boldsymbol{n}_e^- = -\boldsymbol{n}_e^+$ as the unit normal vector to $\boldsymbol{e}$ pointing from K_e^- to K_e^+. In the case where $\boldsymbol{e} \in \partial\Omega$, we set $\boldsymbol{n}_e^+ := \boldsymbol{n}$. We indicate by d_e the distance between $\boldsymbol{x}_{G,K_e^+}$ and $\boldsymbol{x}_{G,K_e^-}$. In the case where $\boldsymbol{e} \in \Gamma$, d_e is the distance between $\boldsymbol{x}_{G,K_e^+}$ and the midpoint of edge $\boldsymbol{e}$.

For each element $K \in \mathcal{T}_h$, we denote by $e(l)$, $l = 1, \ldots, 4$, the label number of edge $\boldsymbol{e}_l$, and by K_l the mesh element neighbor of K with respect to edge $\boldsymbol{e}_l$, whenever $\boldsymbol{e}_l$ does not belong to Γ. For any function $w_h \in \mathbf{Q}_h$, we introduce the two following operators associated with each edge of $\mathcal{E}_h^{\mathrm{in}}$

$$[\![w_h]\!]_e := w^{K_e^+}\boldsymbol{n}_e^+ + w^{K_e^-}\boldsymbol{n}_e^-, \qquad \{w_h\}_e := \frac{1}{2}(w^{K_e^+} + w^{K_e^-}),$$

where for each $K \in \mathcal{T}_h$, w^K is the constant value of w_h over K. The operator $[\![w_h]\!]_e$ is the *jump* of w_h across $\boldsymbol{e}$ while $\{w_h\}_l$ is the *average* of w_h across $\boldsymbol{e}$. The previous definitions apply also in the case where $\boldsymbol{e} \in \partial\Omega$ by setting $w^{K_e^-} := 0$. Finally, let $\boldsymbol{v}$, $\boldsymbol{w}$ be any pair of vectors in $(L^2(\Omega))^2$, and v, w be any function pair in $L^2(\Omega)$. We set $A(\boldsymbol{v}, \boldsymbol{w}) := \int_\Omega a\, \boldsymbol{v} \cdot \boldsymbol{w}$, $B(v, \boldsymbol{v}) := -\int_\Omega v\, \nabla \cdot \boldsymbol{v}$, $C(v, \boldsymbol{v}) := -\int_\Omega v\boldsymbol{\beta} \cdot \boldsymbol{v}$ and $(v, w) := \int_\Omega v\, w$.

Then, the dual mixed finite element approximation of (8) over quadrilateral grids reads: find $u_h \in \mathbf{Q}_h$ and $\boldsymbol{J}_h \in \mathbf{V}_h$ such that, for all $\boldsymbol{\tau}_h \in \mathbf{V}_h$ and for all $q_h \in \mathbf{Q}_h$, we have:

$$A(\boldsymbol{J}_h, \boldsymbol{\tau}_h) + B(u_h, \boldsymbol{\tau}_h) + C(u_h, \boldsymbol{\tau}_h) = 0 \tag{10a}$$
$$B(q_h, \boldsymbol{J}_h) - (q_h, \gamma\, u_h) = -(q_h, f). \tag{10b}$$

Eq. (10a) is the discretized form of the constitutive law (8a), while Eq. (10b) is the discretized form of the conservation law (8b). The finite element pair $\mathbf{Q}_h \times \mathbf{V}_h$ satisfies the *inf–sup* compatibility condition, so that problem (10), under the coerciveness assumption (9), admits a unique solution and optimal error estimates can be proved for the pair $(u_h, \boldsymbol{J}_h)$ in the appropriate graph norm (see [27,21,24]). The DM formulation can be written in matrix form as

$$\begin{bmatrix} \mathbf{A} & (\mathbf{B}^T + \mathbf{C}) \\ \mathbf{B} & \mathbf{D} \end{bmatrix} \begin{pmatrix} \mathbf{j} \\ \mathbf{u} \end{pmatrix} = \begin{pmatrix} \mathbf{0}_{\mathtt{Ned}} \\ \mathbf{f} \end{pmatrix} \tag{11}$$

where $\mathbf{A} \in \mathbb{R}^{\mathtt{Ned}\times\mathtt{Ned}}$ is the flux mass matrix, $\mathbf{B} \in \mathbb{R}^{\mathtt{Nel}\times\mathtt{Ned}}$, $\mathbf{C} \in \mathbb{R}^{\mathtt{Ned}\times\mathtt{Nel}}$, $\mathbf{D} \in \mathbb{R}^{\mathtt{Nel}\times\mathtt{Nel}}$, while $\mathbf{u} \in \mathbb{R}^{\mathtt{Nel}\times 1}$, $\mathbf{j} \in \mathbb{R}^{\mathtt{Ned}\times 1}$ is the unknown vector pair, and $\mathbf{0}_{\mathtt{Ned}}$ is the column null vector of size Ned. The reaction matrix $\mathbf{D}$ is diagonal, while the flux mass matrix $\mathbf{A}$ is symmetric and positive definite and has at most three nonzero entries for each row. Two computational difficulties are associated with the solution of the DM problem (10). The first difficulty is that the linear algebraic system (11) is in saddle-point form and has a considerably larger size than a standard displacement-based method of comparable order. The second difficulty is that, even in the particular case where $\boldsymbol{\beta}$ is equal to zero, it is not possible to ensure that the stiffness matrix acting on the sole variable $\mathbf{u}$ (obtained upon block Gaussian elimination) is an M-matrix for every value of γ (see [28] in the case of triangular RT elements). This implies that the discrete maximum principle (DMP) can be satisfied by the DM method only if the mesh size h is sufficiently small, and this constraint may become even more stringent if convection is present in the model.

4.2. The stabilized dual mixed finite volume approximation

To overcome the above mentioned difficulties, we introduce a (strongly consistent) modification of the DM method that extends to the case of quadrilateral grids the approach for triangular grids proposed and analyzed in [25,26]. The

introduced modifications consist of: (1) replacing the bilinear form $A(\boldsymbol{J}_h, \boldsymbol{\tau}_h)$ with the approximate bilinear form $A_h(\boldsymbol{J}_h, \boldsymbol{\tau}_h)$ obtained by using the trapezoidal quadrature formula; (2) replacing the bilinear form $C(u_h, \boldsymbol{\tau}_h)$ with $C_h(u_h, \boldsymbol{\tau}_h) := C(\{u_h\}, \boldsymbol{\tau}_h)$; (3) adding to the left-hand side of (10a) the stabilization term

$$S(u_h,\ \boldsymbol{\tau}_h) := -\sum_{\boldsymbol{e}\in\mathcal{E}_h^{\text{in}}} \varrho_e(\mathbb{P}e_e)\int_{\boldsymbol{e}} [\![u_h]\!]_e \cdot \boldsymbol{\tau}_h \quad \boldsymbol{\tau}_h \in \mathbf{V}_h, \tag{12}$$

where $\mathbb{P}e_e := (|\boldsymbol{\beta}\cdot\boldsymbol{n}_e|\, d_e)/(2\alpha)$ is the *local Pèclet number* associated with edge $\boldsymbol{e}$ and $\varrho_e : \boldsymbol{e} \in \mathcal{E}_h \to \mathbb{R}^+$ is a stabilization function equivalent to adding, for each edge of $\mathcal{E}_h$, an *artificial diffusion* to the original problem.

To realize the importance of stabilization against possible dominance of the advective term, we estimate the local Pèclet number in the case of the air temperature problem (8). Noting that in computations the mass density ρ_a varies between 1 and 1.2 kg m^{-3}, the air specific heat capacity c_p is almost equal to 1000 J kg^{-1} K^1, the module of the air velocity $|\boldsymbol{v}_a|$ varies between 0.1 and 10 m s^{-1} and the air thermal conductivity k_a varies between 0.025 and 0.03 W m^{-1} K^1, we get

$$1667 d_e \le \mathbb{P}e_e \le 240000 d_e.$$

To prevent the occurrence of spurious oscillations in the computed solution u_h we need to ensure that $\mathbb{P}e_e < 1$, which amounts to requiring the mesh size h to be less than 4 μm. This constraint is extremely demanding in terms of computational resources, so that we introduce the following stabilized DM formulation:
find $u_h \in \mathbf{Q}_h$ and $\boldsymbol{J}_h \in \mathbf{V}_h$ such that, for all $\boldsymbol{\tau}_h \in \mathbf{V}_h$ and for all $q_h \in \mathbf{Q}_h$, we have:

$$A_h(\boldsymbol{J}_h, \boldsymbol{\tau}_h) + B(u_h, \boldsymbol{\tau}_h) + C_h(u_h, \boldsymbol{\tau}_h) + S(u_h,\ \boldsymbol{\tau}_h) = 0 \tag{13a}$$

$$B(q_h, \boldsymbol{J}_h) - (q_h, \gamma\, u_h) = -(q_h, f). \tag{13b}$$

The stabilized DM formulation (13) can be written in matrix form as

$$\begin{bmatrix} \widehat{\mathbf{A}} & (\mathbf{B}^T + \widehat{\mathbf{C}}) \\ \mathbf{B} & \mathbf{D} \end{bmatrix} \begin{pmatrix} \mathbf{j} \\ \mathbf{u} \end{pmatrix} = \begin{pmatrix} \mathbf{0}_{\mathtt{Ned}} \\ \mathbf{f} \end{pmatrix} \tag{14}$$

where $\widehat{\mathbf{A}} \in \mathbb{R}^{\mathtt{Ned}\times\mathtt{Ned}}$ is a *diagonalized* flux mass matrix while $\widehat{\mathbf{C}} \in \mathbb{R}^{\mathtt{Ned}\times\mathtt{Nel}}$ is a stabilized advective flux matrix.

The significant advantage of introducing the modifications (1)–(3) with respect to the standard DM approach is that, for each element $K \in \mathcal{T}_h$, the flux of $\boldsymbol{J}_h$ across the edge $e(l),\ l = 1, \ldots, 4$ (the degree of freedom of $\boldsymbol{J}_h$), can be expressed *explicitly* as a function of the sole degrees of freedom u^K and u^{K_l} as

$$j_{e(l)}(u^K, u_l^K) = \left[-\alpha(1 + \varrho_e(\mathbb{P}e_{e(l)}))\left(\frac{u^{K_l} - u^K}{d_{e(l)}}\right) + \boldsymbol{\beta}\cdot\boldsymbol{n}_{e(l)}\left(\frac{u^K + u^{K_l}}{2}\right)\right]|\boldsymbol{e}_l|. \tag{15}$$

Replacing the above expression into the discrete conservation law (13b), we end up with the stabilized dual mixed-finite volume (MFV) approximation of the model problem (8)

$$\begin{cases} \displaystyle\sum_{l=1}^{4} j_{e(l)}(u^K, u^{K_l}) + u^K\overline{\gamma}_K|K| = \overline{f}_K|K| & \forall K \in \mathcal{T}_h, \\ u^{K_l} = 0 & \boldsymbol{e}_l \in \Gamma, \end{cases} \tag{16}$$

where $\overline{\gamma}_K$ and $\overline{f}_K$ are the mean values of γ and f on K, respectively. The above proposed stabilized MFV method is the extension to rectangular elements of the formulation for triangular grids introduced and analyzed in [25,26]. For a similar use of numerical quadrature aimed to construct a finite volume variant of the DM method, we refer to [29] in the case of the advection–diffusion–reaction model problem and to [30] for the approximate solution of the Stokes problem in fluid-dynamics.

The MFV method (16) can be written in matrix form as

$$\mathbf{K}\mathbf{u} = \mathbf{g} \tag{17}$$

where, for $K = 1, \ldots, \texttt{Nel}$, the entries of the stiffness matrix and of the load vector are:

$$\begin{aligned}
\mathbf{K}_{K,K} &= \sum_{l=1}^{4} \left[\frac{\alpha(1 + \varrho_e(\mathbb{P}e_{e(l)}))}{d_l} + \frac{\boldsymbol{\beta} \cdot \boldsymbol{n}_{e(l)}}{2} \right] |\boldsymbol{e}_l| + \overline{\gamma}_K |K| \\
\mathbf{K}_{K,K_l} &= \left[-\frac{\alpha(1 + \varrho_e(\mathbb{P}e_{e(l)}))}{d_l} + \frac{\boldsymbol{\beta} \cdot \boldsymbol{n}_{e(l)}}{2} \right] |\boldsymbol{e}_l| \\
\mathbf{g}_K &= \overline{f}_K |K|.
\end{aligned} \tag{18}$$

Matrix $\mathbf{K}$ is sparse and has at most five nonzero entries for each row, in the typical format of lowest-order finite volume methods. Proceeding along the same lines as in [25], we can prove the following result.

Proposition 1. *Let the edge artificial viscosity $\varrho_{\boldsymbol{e}}(\mathbb{P}e_{\boldsymbol{e}})$ be chosen in such a way that*

$$\varrho_{\boldsymbol{e}}(\mathbb{P}e_{\boldsymbol{e}}) \geq \mathbb{P}e_{\boldsymbol{e}} - 1 \quad \forall \boldsymbol{e} \in \mathcal{E}_h. \tag{19}$$

Then, $\mathbf{K}$ is an irreducible diagonally dominant M-matrix with respect to its columns [31].

As a consequence of Proposition 1, the MFV scheme (13) satisfies the DMP irrespective of the local convective term *and* mesh size. This lends the scheme a property of robustness which is a significant benefit in industrial computations like those considered in the present article. The simplest choice that allows to satisfy (19) is the upwind stabilization

$$\varrho_l(\mathbb{P}e_{\boldsymbol{e}}) = \mathbb{P}e_{\boldsymbol{e}} \quad \forall \boldsymbol{e} \in \mathcal{E}_h. \tag{20}$$

Another, more elaborate, choice is the so called Scharfetter–Gummel (SG) stabilization

$$\varrho_l(\mathbb{P}e_{\boldsymbol{e}}) = \mathbb{P}e_{\boldsymbol{e}} - 1 + \mathcal{B}(2\mathbb{P}e_{\boldsymbol{e}}) \quad \forall \boldsymbol{e} \in \mathcal{E}_h, \tag{21}$$

where $\mathcal{B}(x) := x/(e^x - 1)$ is the inverse of the Bernoulli function. This latter choice is also known as exponential fitting [32,33]. The two above stabilizations tend to the same limit as the Pèclet number increases. However, their behavior is quite different as the mesh size h decreases, because (20) introduces an artificial diffusion of $\mathcal{O}(h)$ as $h \to 0$ while (21) introduces an artificial diffusion of $\mathcal{O}(h^2)$ as $h \to 0$. For this reason, the SG stabilized MFV formulation is preferable as far as accuracy is concerned, and is the one implemented in the simulations reported in Section 6.

4.3. Numerical validation of the MFV discretization

In this section, we perform a numerical validation of the stabilized MFV method (13) applied to the solution of the model problem (8) with $\Omega = (0, 1) \times (0, 1)$.

In a first case study, we verify the convergence rate of the scheme when $\boldsymbol{\beta} = [0,\ 1]^T$, $\gamma = 1$ and f is computed in such a way that the exact solution is $u(x, y) = \cos x \sin y$. As for the diffusion coefficient, we choose $\alpha = \{1, 10^{-1}, 10^{-2}, 10^{-3}, 10^{-4}\}$, in order to analyze both dominating diffusive and convective regimes. Computations are performed on increasingly refined grids of $N \times N$ square elements of dimension varying from $N = 4$ to $N = 64$. Fig. 6 shows the discrete maximum norm of the discretization error

$$\|u - u_h\|_{\infty,h} := \max_{K \in \mathcal{T}_h} |u(\boldsymbol{x}_{G,K}) - u^K|$$

as a function of α and of the mesh size $h = 1/N$. Results indicate that for low values of the Pèclet number $\mathbb{P}e$, corresponding for example to $\alpha = 1$, the SG method has a convergence order of $\mathcal{O}(h^2)$, that decreases to $\mathcal{O}(h)$ for dominating convection regimes, as for $\alpha = 10^{-4}$. On the other hand, the estimated convergence error of the upwind method is never better than $\mathcal{O}(h)$ for every value of α.

In a second case study, we validate the robustness and accuracy of the SG stabilization in the solution of the two numerical examples considered in [34] where $\alpha = 10^{-6}$, $\gamma = 0$ and $h = 2^{-6}$. In the first example, $f = 1$ and $\boldsymbol{\beta} = [-y, x]^T$. The scope of this computation is to verify the accuracy and stability of the method in managing a boundary layer without introducing spurious oscillations. In the second example, $f = 0$ and $\boldsymbol{\beta} = \nabla\psi$, ψ being the

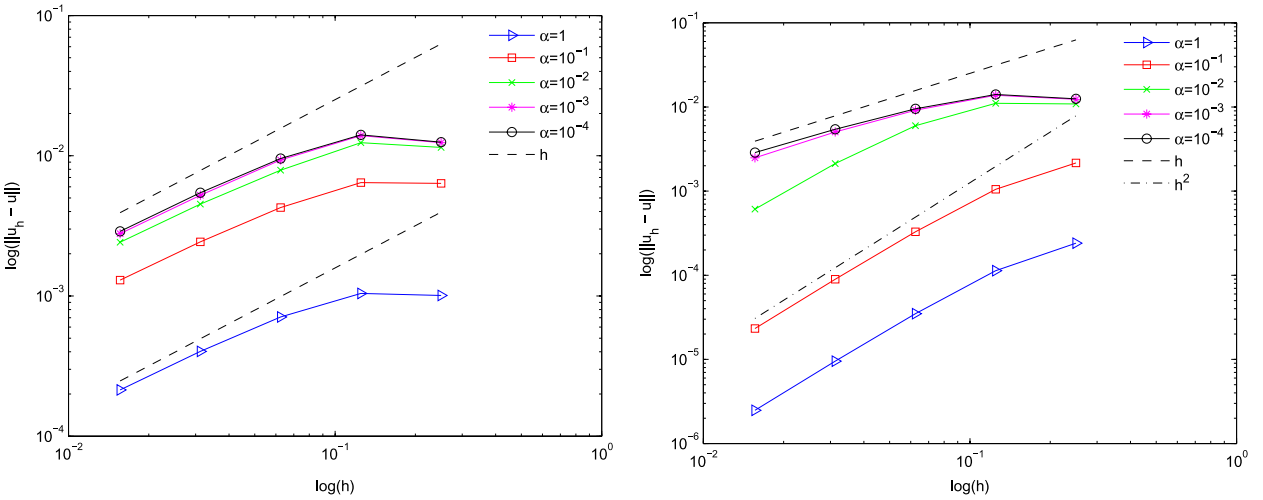

(a) Upwind stabilization.

(b) SG stabilization.

Fig. 6. Logarithmic plot of the maximum norm of the discretization error as a function of h and α.

potential function defined as

$$\psi = \begin{cases} 0 & 0 \le d + x < 0.55, \\ 2(d - 0.55) & 0.55 \le d + x < 0.65, \\ 0.2 & 0.65 \le d + x, \end{cases}$$

where $d = (x^2 + y^2)^{1/2}$. Mixed Dirichlet–Robin conditions are enforced on the boundary Γ in such a way that the solution exhibits two interior layers, one of which is very sharp. For graphical purposes, the computed values of u_h have been interpolated through a nodally continuous function. Results reported in Fig. 7 are in excellent agreement with those of [34] and demonstrate the robustness of the stabilized MFV method with respect to dominating convective terms and its ability in capturing sharp boundary and interior layers without introducing any spurious oscillation in accordance with Proposition 1.

5. Primal mixed discretization of the 1D fluid equations

In this section we focus on the description of the Primal Mixed (PM) finite element scheme for the discretization of the two-phase fluid equations (2). The choice of the primal-mixed finite element method is due to the fact that, in its lowest order form, it enforces a weak flux continuity across interelement boundaries with a piecewise linear continuous approximation of the scalar unknown that makes it structurally similar to standard displacement-based finite element schemes. A sound theoretical foundation (see [35] for an introduction and analysis), confirmed by the included computational experiments, is another important motivation for selecting the PM approach in the discretization of (2). Finally, it is worth noting that while the use of PM methods is well established in the numerical solution of elliptic boundary value problems, it is not so common for the treatment of problems with a markedly advective character like those considered in this section and thus makes the PM method an attractive scheme for the finite element approximation of the model system (2).

5.1. *Primal mixed finite element approximation*

In the following, we consider one pipe only and drop the subscript denoting the pipe being considered. We start by noting that both (3) and (4) are special instances of the following boundary value problem to be solved in the 1D domain $\sigma = (0, L)$:

$$\partial_s J = f \tag{22a}$$

$$-\varepsilon \partial_s u + \beta u = J + g \tag{22b}$$

$$u(0) = u(L) = 0 \tag{22c}$$

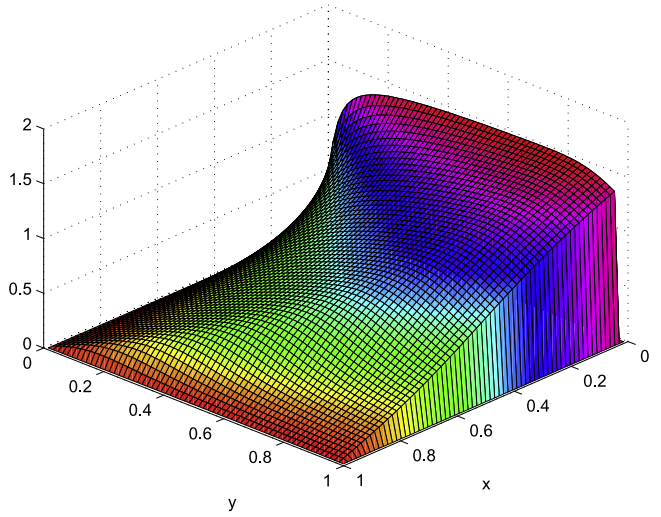

(a) Boundary layer example.

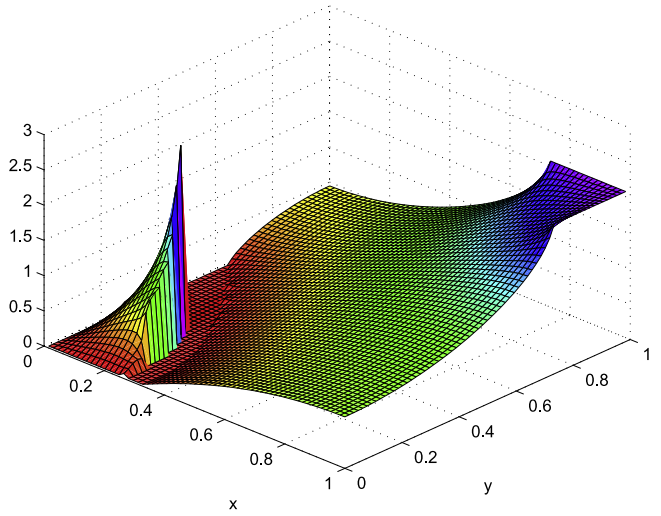

(b) Interior layer example.

Fig. 7. Surface plot of the numerical solution of two problems with sharp boundary and interior layers.

where f, β and g are given data, and ε is a non-negative diffusion coefficient. We recover (3) by setting $J = -G$, $u = \varphi$, $\varepsilon = R^{-1}$, $g = -R^{-1}\rho\mathbf{g}\cdot\mathbf{d}$, $f = 0$ and $\beta = 0$, while we recover (4) by setting $J = \mathcal{W}$, $u = \mathcal{H}$, $\varepsilon = 0$, $g = 0$, $f = h_{wc}(T_w - T_c)$ and $\beta = G$.

Remark 1 (*Purely Advective Character of the Two-Phase Fluid Model*)**.** From the mathematical point of view, the model problem (22) represents an advective–diffusive model in conservation form quite similar to that introduced in Section 4 for the description of the air/panel physical model. In the present case, however, there is an important difference because the two-phase fluid equations (2) have a *purely advective* character so that the introduction of a diffusive term in the model system (22) must be regarded as a stabilization term for the corresponding numerical discretization of Eqs. (2). For this reason, throughout the section, we always assume ε to be strictly positive.

Remark 2 (*Extension to Pipeline Geometry*)**.** The advective–diffusive model (22) is here solved in the interval $\sigma = (0, L)$ only for ease of presentation of the Primal Mixed Finite Element Method approximation. The incorporation

of the coupling conditions (5) at each junction node of the pipeline network is straightforward with the adopted discretization scheme and is discussed in detail in the remainder of the section.

Let ε be a positive bounded function and set $a := \varepsilon^{-1}$. Then, the advective–diffusive problem (22) can be written in mixed form as:
find $u : \sigma \to \mathbb{R}$ and $J : \sigma \to \mathbb{R}$ such that:

$$aJ + \partial_s u - a\beta u + ag = 0 \qquad \text{in } \sigma, \tag{23a}$$
$$\partial_s J = f \qquad \text{in } \sigma, \tag{23b}$$
$$u(0) = u(L) = 0. \tag{23c}$$

We assume that

$$\partial_s(a\beta) \geq 0 \quad \text{a.e. in } \sigma. \tag{24}$$

In view of the numerical approximation of (23) we introduce a partition $\mathcal{T}_h$ of σ into N intervals K_i of length h_i, $i = 1 \dots N$, by means of $N + 1$ nodes s_j, $j = 0 \dots N, s_0 = 0, s_N = L$. We also introduce the following function spaces defined on $\mathcal{T}_h$:

$$V_h = \left\{ v_h \in C^0(\overline{\sigma}) : v_h|_{K_i} \in \mathbb{P}_1(K) \, \forall K \in \mathcal{T}_h, \; v_h(0) = v_h(L) = 0 \right\}$$
$$Q_h = \left\{ p_h \in L^2(\sigma) : p_h|_{K_i} \in \mathbb{P}_0(K) \, \forall K \in \mathcal{T}_h \right\}.$$

Functions in V_h are piecewise linear continuous over $\overline{\sigma}$ and vanish at the boundary $\partial\sigma$ while functions in Q_h are piecewise constant over σ. Nodal continuity of functions in V_h ensures the automatic satisfaction of the coupling conditions (5a) and (5b).

The PM finite element approximation of (23) reads:
find $u_h \in V_h$ and $J_h \in Q_h$ such that:

$$A(J_h, q_h) + B(u_h, q_h) + C(u_h, q_h) = -(ag, q_h) \qquad \forall q_h \in Q_h \tag{25a}$$
$$B(v_h, J_h) = -(v_h, f) \qquad \forall v_h \in V_h, \tag{25b}$$

where

$$A(J_h, q_h) := \int_\sigma a \, J_h \, q_h \, ds,$$
$$B(v_h, J_h) := \int_\sigma J_h \, \partial_s v_h \, ds,$$
$$C(u_h, q_h) := -\int_\sigma a \, \beta \, u_h \, q_h \, ds$$

and $(\cdot, \cdot)$ denotes the scalar product in $L^2(\sigma)$. It can be checked that under the coercivity assumption (24), problem (25) is uniquely solvable.

The PM system (25) can be written in matrix form as

$$\begin{bmatrix} \mathbf{A} & (\mathbf{B}^T + \mathbf{C}) \\ \mathbf{B} & \mathbf{0} \end{bmatrix} \begin{pmatrix} \mathbf{j} \\ \mathbf{u} \end{pmatrix} = \begin{pmatrix} \mathbf{g} \\ \mathbf{f} \end{pmatrix} \tag{26}$$

where $\mathbf{A} \in \mathbb{R}^{N \times N}$ is the flux mass matrix, $\mathbf{B} \in \mathbb{R}^{(N-1) \times N}$ and $\mathbf{C} \in \mathbb{R}^{N \times (N-1)}$, while $\mathbf{u} \in \mathbb{R}^{(N-1) \times 1}$, $\mathbf{j} \in \mathbb{R}^{N \times 1}$ is the unknown vector pair, and $\mathbf{0} \in \mathbb{R}^{(N-1) \times (N-1)}$ is the null square matrix of size $N - 1$. Compared with the dual mixed system (11), the PM formulation (26) has a considerable advantage because matrix $\mathbf{A}$ is *diagonal*, each diagonal entry A_{kk} corresponding to the element K_k in the grid, $k = 1, \dots, N$. Assuming that ε, β and g are constant over each element K_i, the first equation of (25) can be solved for the flux J_h over each mesh element

$$J_k = -\varepsilon_k \frac{u_k - u_{k-1}}{h_k} + \beta_k \frac{u_{k-1} + u_k}{2} - g_k \quad \forall i = k, \dots, N. \tag{27}$$

Taking v_h equal to the "hat" function φ_i, equal to 1 at every internal node s_i and zero at every other node, $i = 1, \ldots, N-1$, we end up with the following system of *nodal conservation laws*:

$$J_{i+1} - J_i = f_i \left(\frac{h_i + h_{i+1}}{2} \right) \quad i = 1, \ldots, N-1. \tag{28}$$

The above equation expresses the fact that at each internal node of the partition the output flux J_{i+1} is equal to the sum of the input flux J_i plus the nodal production term $P_i := f_i(h_i + h_{i+1})/2$, in strong analogy with the classical Kirchhoff law for the current in an electric circuit. In particular, if $f = 0$, we get strong flux conservation at the node s_i, $i = 1, \ldots, N-1$, which corresponds to enforcing in strong form the coupling conditions (5c) and (5d).

Substituting (27) into (28) we end up with the linear algebraic system in the sole variable u_h

$$\mathbf{MU} = \mathbf{F} \tag{29}$$

where $\mathbf{U} \in \mathbb{R}^{(N-1)\times 1}$ is the vector of nodal dofs for u_h, $\mathbf{F} \in \mathbb{R}^{(N-1)\times 1}$ is the right-hand side and $\mathbf{M} \in \mathbb{R}^{(N-1)\times(N-1)}$ is the stiffness matrix whose entries are given by:

$$M_{ij} = \begin{cases} -\dfrac{\varepsilon_i}{h_i} - \dfrac{\beta_{i+1}}{2} & j = i-1 \\ \dfrac{\varepsilon_i}{h_i} + \dfrac{\varepsilon_{i+1}}{h_{i+1}} + \dfrac{\beta_{i+1}}{2} - \dfrac{\beta_i}{2} & j = i \\ -\dfrac{\varepsilon_{i+1}}{h_{i+1}} + \dfrac{\beta_{i+1}}{2} & j = i+1. \end{cases}$$

As in the case of the dual mixed method of Section 4.1, the matrix $\mathbf{M}$ turns out to be an M-matrix only if the mesh size h is sufficiently small. To avoid this inconvenience, we define the local Pèclet number

$$\mathbb{P}e_i := \frac{|\beta_i| h_i}{2\varepsilon_i} \quad i = 1, \ldots, N$$

and modify the PM finite element scheme by simply replacing in the first equation of (25) the term $a = \varepsilon^{-1}$ with

$$a_h|_{K_i} := (\varepsilon_i(1 + \mathbb{P}e_i))^{-1} = \left(\varepsilon_i + \frac{|\beta_i| h_i}{2} \right)^{-1} \quad i = 1, \ldots, N.$$

This amounts to adding a stabilizing artificial diffusion term of upwind type (cf. (20)) into the method and transforms system (29) into the stabilized PM scheme

$$\mathbf{M}^{\text{stab}}\mathbf{U} = \mathbf{F} \tag{30}$$

where the entries of the stiffness matrix $\mathbf{M}^{\text{stab}}$ of the stabilized PM method now read:

$$M_{ij}^{\text{stab}} = \begin{cases} -\dfrac{\varepsilon_i}{h_i} - \beta_i^+ & j = i-1 \\ \dfrac{\varepsilon_i}{h_i} + \dfrac{\varepsilon_{i+1}}{h_{i+1}} + \beta_{i+1}^+ - \beta_i^- & j = i \\ -\dfrac{\varepsilon_{i+1}}{h_{i+1}} + \beta_{i+1}^- & j = i+1 \end{cases}$$

having set:

$$\beta^+ := \frac{\beta + |\beta|}{2} \quad (\geq 0)$$
$$\beta^- := \frac{\beta - |\beta|}{2} \quad (\leq 0).$$

By inspection on the expressions of M_{ij}^{stab} we have the following result.

Proposition 2. *The stiffness matrix* $\mathbf{M}^{\text{stab}}$ *is an irreducible diagonally dominant* M*-matrix with respect to its columns.*

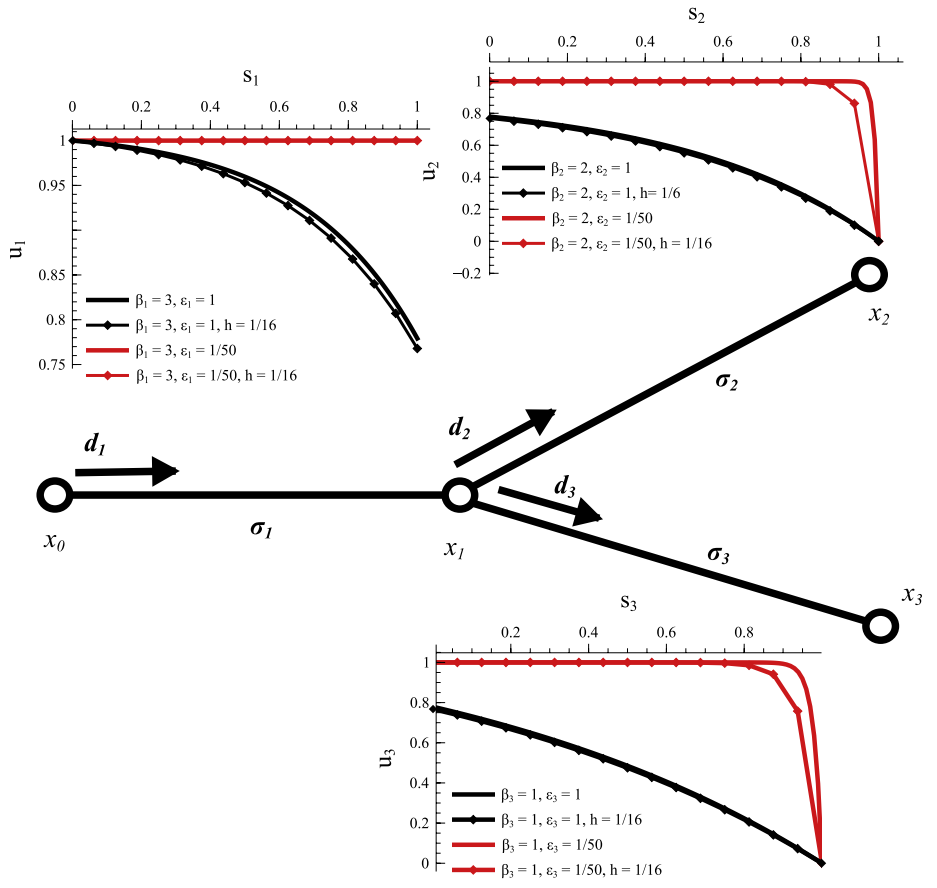

Fig. 8. Test case on a three-segment network. Solid lines denote the exact solution while dotted lines denote the numerical solution computed by the upwind stabilized PM method.

As in the case of the MFV scheme, Proposition 2 implies that the upwind stabilized PM finite element scheme satisfies the DMP. Moreover, the upwind PM method is at most first-order accurate with respect to the discretization parameter h.

Remark 3 (*Stabilization Method*)**.** In the case of problem (4) the SG stabilization (21) cannot be used because $\varepsilon = 0$. Therefore, to ensure a consistent treatment that is applicable in both hyperbolic and advective–diffusive regimes, the artificial diffusion term of upwind type (20) is added in the numerical examples of Sections 5.2 and 6.

5.2. Numerical validation of the PM discretization

In this section, we perform a numerical validation of the stabilized PM method (30) applied to the solution of the model problem (22) on the test network geometry depicted in Fig. 8.

In the first test case we study a diffusion-dominated flow while in the second test case the flow is in the advection-dominated regime. For both cases we let $\beta|_{\sigma_1} = 3$, $\beta|_{\sigma_2} = 2$, $\beta|_{\sigma_3} = 1$ and $f = g = 0$. For the first test case, whose exact solution is shown in black in Fig. 8, we let $\varepsilon = 1$ on all network segments, while for the second test, whose exact solution is shown in red in Fig. 8, we let $\varepsilon = 1/50$. It is easily verified that the exact solution of both tests can be expressed as:

$$u(s)|_{\sigma_i} = u(0)|_{\sigma_i} \frac{e^{(\beta|_{\sigma_i} L_i)/\varepsilon} - e^{(\beta|_{\sigma_i} s)/\varepsilon}}{e^{(\beta|_{\sigma_i} L_i)/\varepsilon} - 1} + u(L_i)|_{\sigma_i} \frac{e^{(\beta|_{\sigma_i} s)/\varepsilon} - 1}{e^{(\beta|_{\sigma_i} L_i)/\varepsilon} - 1} \tag{31a}$$

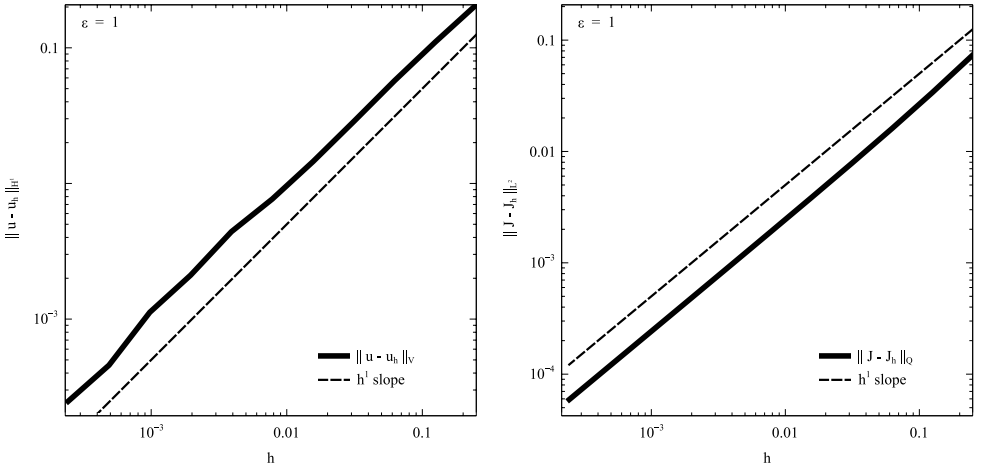

(a) $\|u - u_h\|_V$. (b) $\|J - J_h\|_Q$.

Fig. 9. Logarithmic plot of the discretization error as a function of h in the case $\varepsilon = 1$.

$$J(s)|_{\sigma_i} = \beta|_{\sigma_i} \frac{u(0)|_{\sigma_i} e^{(\beta|_{\sigma_i} L_i)/\varepsilon} - u(L_i)|_{\sigma_i}}{e^{(\beta|_{\sigma_i} L_i)/\varepsilon} - 1} \tag{31b}$$

for $i = 1, 2, 3$, where $L_1 = L_2 = L_3 = 1, u(0)|_{\sigma_1} = 1, u(L_1)|_{\sigma_1} = u(0)|_{\sigma_2} = u(0)|_{\sigma_3} = \omega$ and $u(L_2)|_{\sigma_2} = u(L_3)|_{\sigma_3} = 0$. The value ω of the solution u at the junction node x_1 is determined from the flux continuity condition

$$J|_{\sigma_1} = J|_{\sigma_2} + J|_{\sigma_3},$$

that yields

$$\omega = \frac{\frac{\varepsilon}{L_1}\mathcal{B}\left(\frac{-\beta|_{\sigma_1} L_1}{\epsilon}\right) u(0)|_{\sigma_1} + \frac{\varepsilon}{L_2}\mathcal{B}\left(\frac{\beta|_{\sigma_2} L_2}{\epsilon}\right) u(L_2)|_{\sigma_2} + \frac{\varepsilon}{L_3}\mathcal{B}\left(\frac{\beta|_{\sigma_3} L_3}{\epsilon}\right) u(L_3)|_{\sigma_3}}{\frac{\varepsilon}{L_1}\mathcal{B}\left(\frac{\beta|_{\sigma_1} L_1}{\epsilon}\right) + \frac{\varepsilon}{L_2}\mathcal{B}\left(\frac{-\beta|_{\sigma_2} L_2}{\epsilon}\right) + \frac{\varepsilon}{L_3}\mathcal{B}\left(\frac{-\beta|_{\sigma_3} L_3}{\epsilon}\right)}$$

where $\mathcal{B}$ is the inverse of the Bernoulli function introduced in Section 4.2.

Fig. 9 shows the logarithmic plots of the discretization errors $\|u - u_h\|_V$ and $\|J - J_h\|_Q$ as a function of the discretization parameter h in the diffusive-dominated regime. The scheme turns out to have a first-order accuracy. This result confirms the validity of the error analysis carried out in [35] in the case of a purely diffusive problem also in the case of an advective–diffusive model.

Fig. 10 shows the logarithmic plots of the discretization errors $\|u - u_h\|_V$ and $\|J - J_h\|_Q$ as a function of the discretization parameter h in the advective-dominated regime. The scheme is still first-order accurate with respect to h in the computation of the primal variable u despite the fact that the magnitude of the computed error is higher than in the diffusion-dominated regime. The reported error curve for the flux variable J is dominated by the effect of round-off, in accordance with the fact that in the advective-dominated regime the flow is almost hyperbolic and the computed flux J_h is a very good approximation of the exact flux J.

We conclude the validation analysis of the upwind stabilized PM method by considering again Fig. 8 which shows the numerical solution of the benchmark problem (denoted by black and red dotted curves) computed with a grid spacing $h = 1/16$ and superposed to the exact solution (31a). It is to be noted that in the advective-dominated regime ($\varepsilon = 1/50$) the numerical solution almost coincides with the exact one in the first branch of the network σ_1 because there the problem is almost hyperbolic and the input datum $u(0) = 1$ is transported by the fluid velocity. We also note that in the other two branches of the network, σ_2 and σ_3, even though the chosen stepsize is not sufficiently small to fully resolve the boundary layer at the outlets, the PM upwind method provides a solution which is monotone and free of spurious oscillations in accordance with Proposition 2. A more considerable error occurs in the computed solution when the problem is diffusion-dominated ($\varepsilon = 1$) in accordance with the fact that the PM is only first-order accurate.

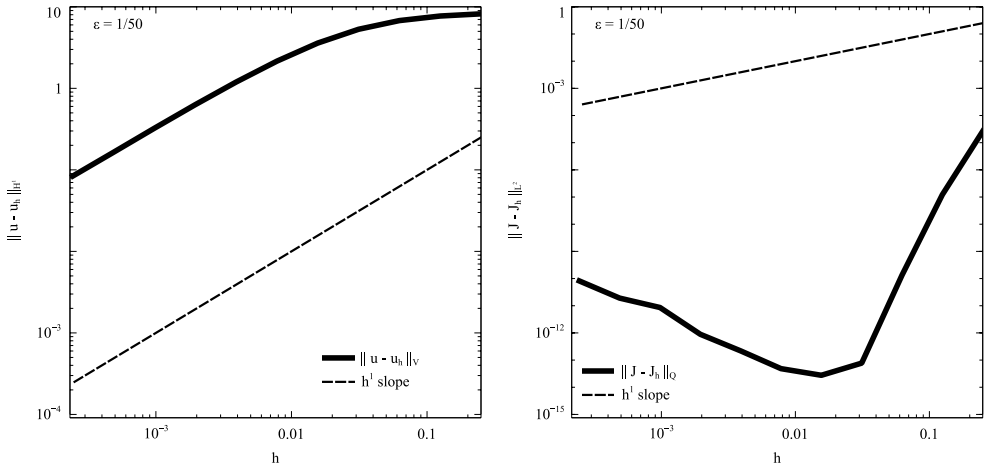

(a) $\|u - u_h\|_V$. (b) $\|J - J_h\|_Q$.

Fig. 10. Logarithmic plot of the discretization error as a function of h in the case $\varepsilon = 1/50$.

Table 1
Model parameters.

Parameter	Value	Units
S	0.05	m
$\lambda_1 = \lambda_2$	0.025	m
T_a^{in}	298.15	K
$\lvert \boldsymbol{V}_a^{\text{in}} \rvert$	1	m s^{-1}
W	0.45	m
H	0.2	m
T_0	358.15	K
G_{tot}	5.8	$\text{kg m}^{-2}\,\text{s}^{-1}$
h_{wc}	3	$\text{W m}^{-2}\,\text{K}^{-1}$
h_{aw}	1.1	$\text{W m}^{-2}\,\text{K}^{-1}$

6. Simulation results

In this section we perform a thorough validation of the computational model illustrated in the previous sections. The simulations are representative of realistic geometries of advanced cooling systems for power electronics. In particular aluminum condenser panels, as part of a two-phase thermosiphon loop, are simulated in natural convection operation mode. In Section 6.1 we analyze the impact of channel geometry and topology on the cooling performance, while in Section 6.2 we compare the model predictions with the measured data reported in [2] and based on the experimental campaign and methodology illustrated in [1].

6.1. Comparison of different channel geometries

In this section we use our simulation code to estimate the impact of different pipe geometries on the cooling properties of the system. With this aim, we consider three test cases where panel size and material, input power, air velocity and temperature are the same, but with different channel paths.

The developed code represents a strong tool in the design of complex channel geometries allowing the researchers to optimize the topology of complex systems.

The simulation data are summarized in Table 1.

The total mass of coolant flowing through the panel per unit time is given by the user as an input datum of the simulation and is equal to G_{tot} multiplied by the value of the pipe cross-sectional area. The coolant is assumed to be in full vapor state at the inlet of the system.

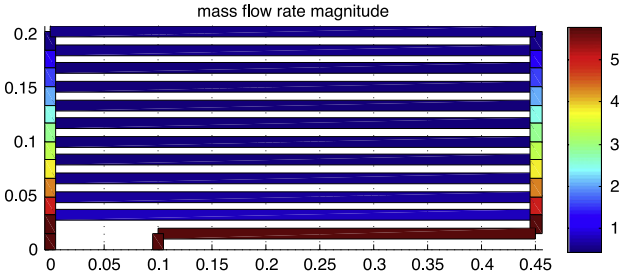

(a) Device A.

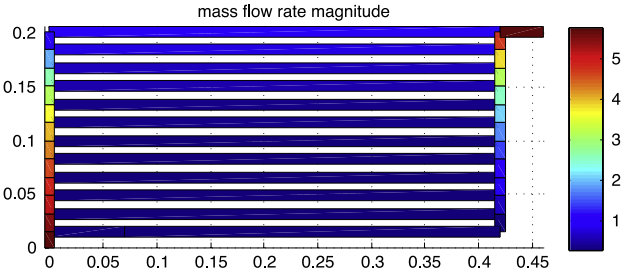

(b) Device B.

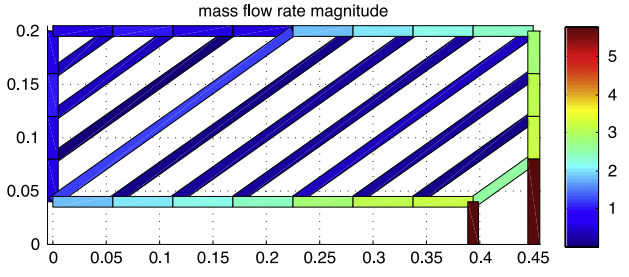

(c) Device C.

Fig. 11. Comparison of mass flow rate magnitude for the three devices geometries.

The geometry of the three devices is compared in Fig. 11, with the color scale representing the absolute value of the mass flow rate in each channel segment.

The structure of a condenser panel is based on a series of parallel channels. A good flow distribution is a mandatory element for an optimal design, allowing the designer to maximally exploit the system and therefore increasing the maximum power density of the cooling device. Case “a” and case “b” indicate a better distribution of mass flow over the parallelized channels compared to case “c”. Starting from case “a” and “b”, we see that the flow distribution is a function of the flow-path resistance: the higher the flow-path resistances, the lower is the flow rate. For case “a”, the flow rate is higher in the lower channels, closer to the inlet, and slightly decreases toward the top part of the panel. The configuration “b” is a possible design solution to overcome the pressure drop unbalance that may occur among the channels, and to guarantee a more uniform distribution over the entire surface due to equal inlet–outlet channel-flow-path length. Unfortunately, this effect is not present and a distribution of the mass flow rate similar to that in case “a” is obtained. Case “c” is studied to take advantage of the channel orientation and the positive effect of the gravitational field in the condensation process.

While the effect of gravity due to channel orientation helps reducing the pressure losses across the system, the short channels close to the flow inlet act as short circuit path, allowing high mass flow rates of vapor directly from inlet to outlet. This has the clear disadvantage that high flow rates of vapor cannot condense efficiently over a short distance. The described mass flow rate distribution has a strong effect on the local vapor quality, as depicted in Fig. 12. Generally, for a channel of fixed length, high flow rates correspond to a high vapor quality at the discharge.

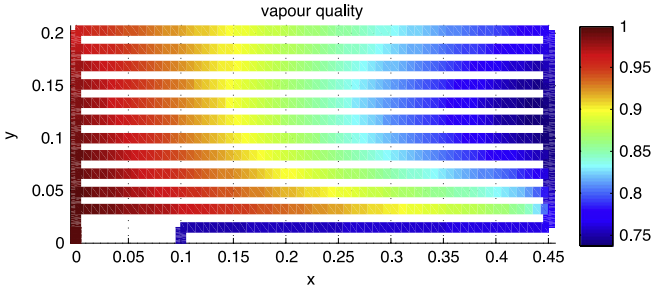

(a) Device A.

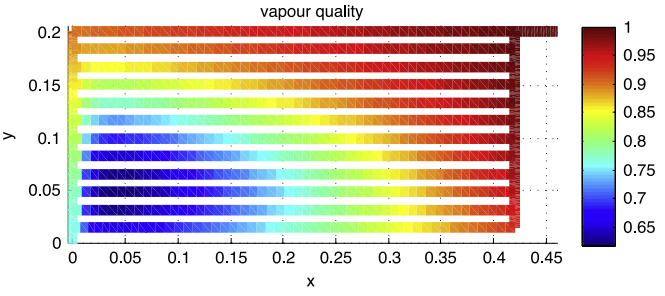

(b) Device B.

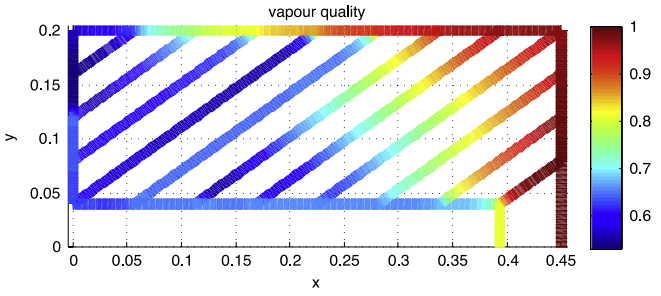

(c) Device C.

Fig. 12. Comparison of vapor quality for the three devices geometries.

This phenomenon is particularly evident in case “c”, where the lower sub-channel with the higher flow rate does not provide a good condensation due to its short length. The designer should seek for a balanced distribution of the vapor qualities at the discharge of each channel in order to exploit best the heat transfer area.

Fig. 13 shows the value of the panel temperature for the three different geometries. Results indicate an almost constant temperature distribution. This is the characteristic of a two-phase system where the condensation heat transfer coefficients are orders of magnitude higher than those of the air side.

Fig. 14 shows the distribution of the air temperature for the three different geometries. This plot is a visual representation of the total heat released by the panel to the ambient and contributing to the sensible heating of the air stream, and provides the designer a clear and precious information on the “goodness” of the thermal performance of the cooling device. Considering the original boundary condition of a fixed inlet mass flow rate of vapor, a higher air temperature difference indicates a higher amount of transferred heat. While case “a” and case “b” are comparable, case “c” shows a lower air temperature at the discharge of the panel, clearly indicating a lower heat transfer to the air. This is well supported by the mass flow rate distribution and vapor quality plots. We also can notice that in Fig. 14 the air temperature differences are smaller in case “c” compared to “a” and “b”. This is probably to be ascribed to the fact that a mass flux is enforced as boundary condition in the simulation model (mass flow rate of vapor per unit area) and not power.

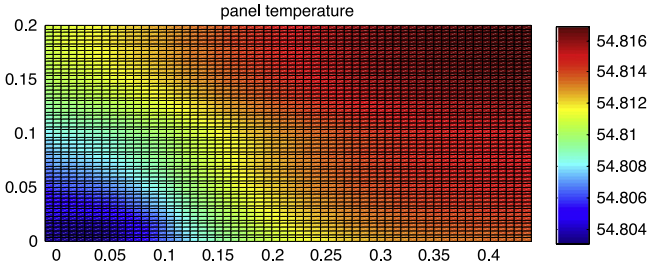

(a) Device A.

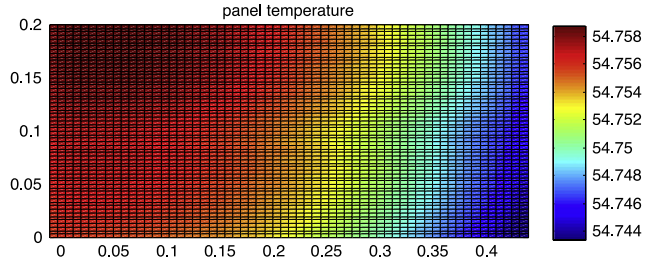

(b) Device B.

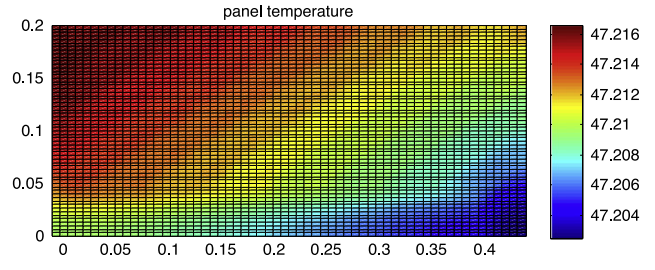

(c) Device C.

Fig. 13. Comparison of panel temperature for the three device geometries.

Fig. 15 shows the spatial distribution of the so called two phase density or bulk density for the three different device geometries. This quantity represents a weighted density between liquid and vapor densities, the weighting factor being the vapor quality. This means that the bulk density is the sum of the vapor and liquid densities multiplied by the vapor quality (vapor phase fraction) and its complement (liquid phase fraction), respectively. As a result, portions of the channels with higher bulk densities represent a fluid in a state with a higher content of liquid phase. To interpret Fig. 15 we can directly refer to Fig. 12, so that high flow rates imply a high vapor quality at the discharge and relatively low two phase densities. As discussed for Fig. 12, this latter phenomenon is particularly evident in case "c" where the lower sub-channel with the higher flow rate does not provide a good condensation due to its short length and low vapor densities occur. As for the vapor quality, the design should seek for a balanced distribution of the two phase densities at the discharge of each channel in order to exploit at the best the heat transfer area and in order to have a balanced distribution of the liquid and vapor phases across the condensing panel.

6.2. Comparison with measured data

In this section we carry out a set of simulation runs to validate the performance of the computational model on realistic geometries and fluid-dynamical data. The experimental campaign and test set-up used for the validation follows closely what is presented in [1,2]. As described in [2], the investigated cooling system is a thermosiphon device constituted of: an evaporator body, a vapor riser, a condenser (stack of roll-bonded panels) and a liquid downcomer. The evaporator can accommodate two ABB HighpakTM power semiconductor modules. Once the modules are in

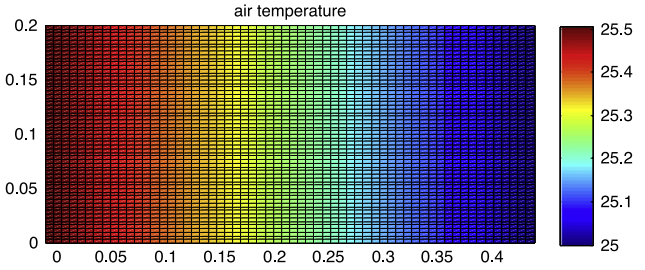

(a) Device A.

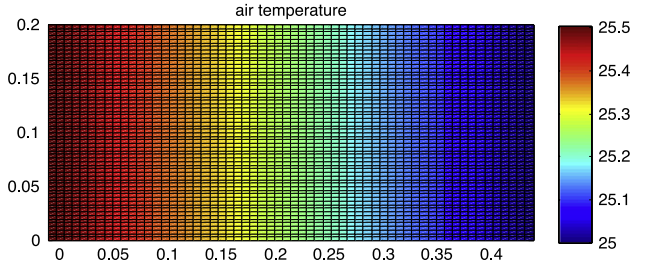

(b) Device B.

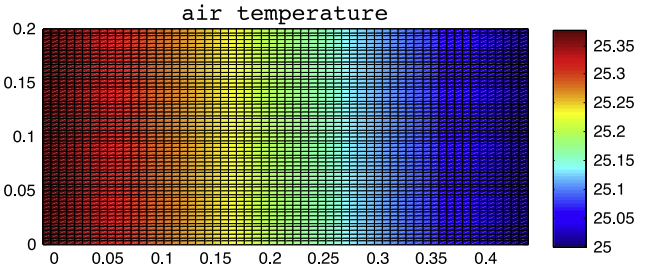

(c) Device C.

Fig. 14. Comparison of air temperature for the three device geometries.

operation the evaporator collects the heat transferred by means of an evaporating fluid. The evaporator is designed in such a way that at its discharge the liquid is separated from the vapor. The liquid is brought back to the evaporator inlet while the vapor travels toward the condenser through the vapor riser. At the inlet of the condenser a vapor distributor feeds the stack of aluminum panels, equally distributing the mass flow among them. The panels are so-called roll-bonded panels, constituted of two aluminum sheets bounded together over almost the entire surface. Where this bounding is not present, a channel is generated, allowing the passage of the two-phase flow. The heat is rejected to the ambient by means of natural convection, the vapor is brought back to liquid conditions. Finally, the liquid is driven back to the evaporator inlet by gravity. The same aluminum panels and stack geometrical layout as presented in [2] are the subject of the investigation. The condenser is a stack of 13 panels 500 mm wide and 250 mm high, 1.2 mm thick, and equally spaced with a pitch of 18 mm. Each panel contains 11 horizontal flow channels of a nominal length of 390 mm. The flow channel is formed on both sides of the panel with isosceles trapezoidal sections, the base and the height measuring 10 mm and 2.1 mm, respectively. The vapor and liquid phases are distributed to and collected from the panels by means of collectors of 19 and 16 mm internal diameter, respectively. Detailed drawings are available in [2], while a detailed description of the experimental measurement techniques is presented in [1]. The experimental conditions are summarized in Table 2.

Fig. 16 presents the computed panel temperature corresponding to a power inflow of 1500 W, air inlet temperature of 25 °C and natural convection operation. It is observed that the panel is almost isothermal. This is the characteristic of the investigated system. A condensing fluid in the panel channels is characterized by high heat transfer coefficients,

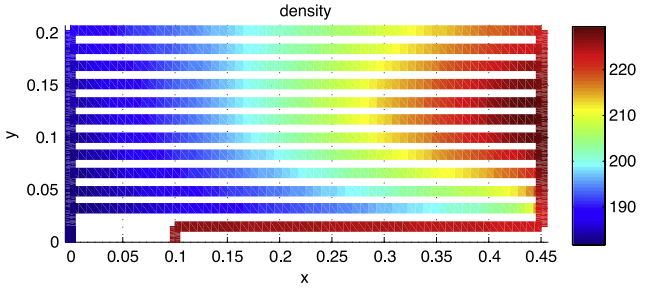

(a) Device A.

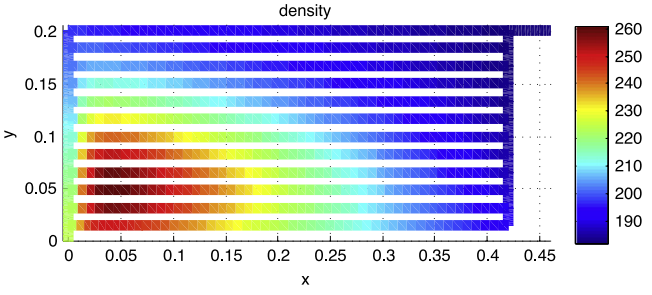

(b) Device B.

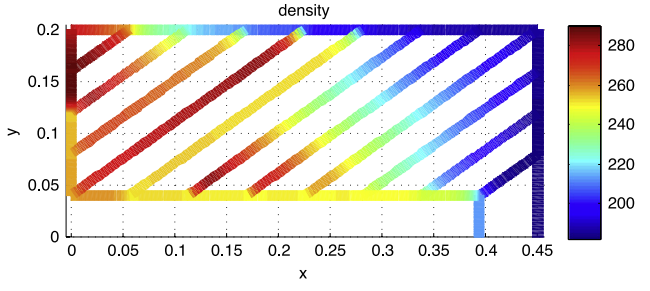

(c) Device C.

Fig. 15. Comparison of the density of the two phase fluid for the three device geometries.

Table 2
Experimental conditions.

Fluid	R245fa
Refrigerant charge	2 kg
Filling ratio	0.5
Heat load	200–1600 W
Ambient temperature	298.15 K
Air cooling regime	Natural convection

orders of magnitude higher than heat transfer coefficients typical of natural convection in air. The heat transfer conditions as well as the nature of the panel, sufficient thickness, small distance between channels and relatively high thermal conductivity of the aluminum result in an almost constant panel temperature. An almost constant temperature of the condenser panel is what we are looking for from an application point of view. It allows to overcome a common drawback of a standard heat-sink based system, where the metallic fin does not behave as a perfect fin (constant temperature) but has a temperature gradient from base to tip, resulting in a limited efficiency. Having an almost constant temperature results in an efficiency of the fin close to unity. The panel border is the coldest part. The low

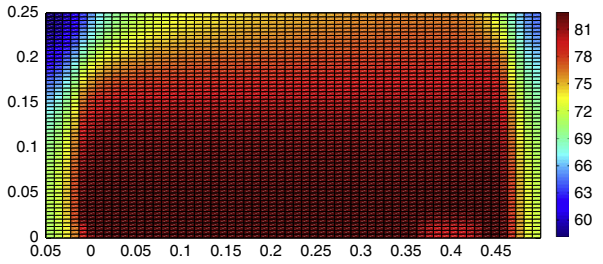

Fig. 16. Computed panel temperature for a total dissipated power of 1500 W.

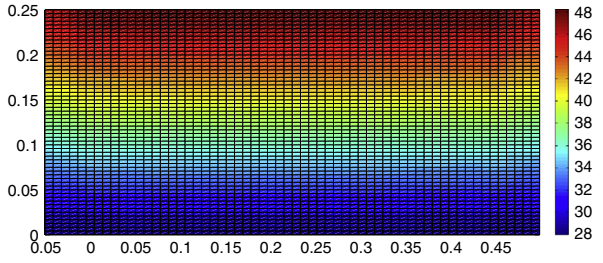

Fig. 17. Computed air temperature for a total dissipated power of 1500 W.

temperature in this region is due to boundary effects. While the rest of the panel has an almost constant temperature, we can still identify a hotter region in the lower part of the panel compared to the top part.

Fig. 17 depicts the air temperature between two panels. The values are averaged in the direction perpendicular to the panel surface. The temperature pattern is the characteristic of the transfer of sensible heat from panel to air in natural-convection operation. The large temperature difference between inlet and outlet of the condenser panel results from the small air velocity typical of natural convection. The maximum allowed temperature difference between inlet and outlet is usually a design parameter, and the designer of the device tries to optimize the system in order to match this value. A higher allowed temperature difference makes it possible to shrink the size of the device. On the other hand, when required, a decrease of the maximum temperature difference can be obtained by increasing the number of panels or the panel area. Since the panel temperature decreases from bottom to top, while the air temperature increases in that direction, the temperature difference between air and panel is largest at the panel bottom. This means that the heat flux from panel to air is maximum at the panel bottom.

The mass flow rate distribution among the panel channels plays an important role in the behavior of the condenser. During operation, the two-phase fluid tends to flow in the horizontal channels suitably paralleled. Considering the fact that the flow path through the panel and hence the flow resistance is smallest for the bottom channel, a decrease in mass flow rate from bottom to top is expected. A certain inhomogeneity in mass flow rate must therefore always be accounted for in the type of parallel connection of channels. Due to the higher mass flow rate, and consequently higher velocity in the bottom channel, a lower fluid residence time per channel length results. Consequently, it is expected that a longer channel length is needed to complete condensation.

This is indeed observed in the simulation results in Fig. 18, showing the local vapor quality in the channels. For the bottom channel, a longer distance from the channel inlet is needed for the vapor quality to decay to a certain value. Consequently, the vapor quality at the channel end, i.e. at the left in the figure, is highest for the bottom channel and lowest for the top channel. Furthermore, from the energy balance, it is clear that the condensation of the highest mass flow rate in the bottom channel requires the largest heat flow rate from channel to air. Since all channels have the same surface area, one expects the heat flux to be highest for the bottom channel and lowest for the top channel. This closely agrees with the observation of maximum temperature difference between panel and air at the bottom and the corresponding maximum heat flux between panel and air in this region.

The designer may try to minimize the observed differences in performance between the condenser channels by optimizing the channel design. For example, one may try to achieve the same vapor quality at the end of all condenser channels. Complete condensation and hence low vapor quality is fundamental to guarantee a safe and

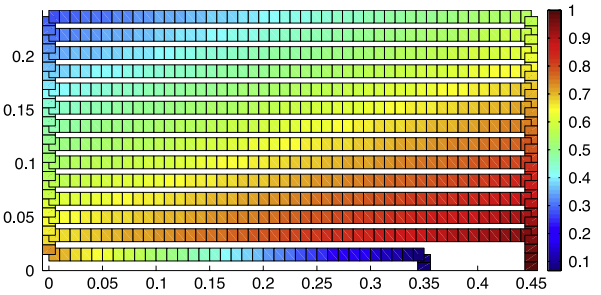

Fig. 18. Computed refrigerant vapor quality for a total dissipated power of 1500 W.

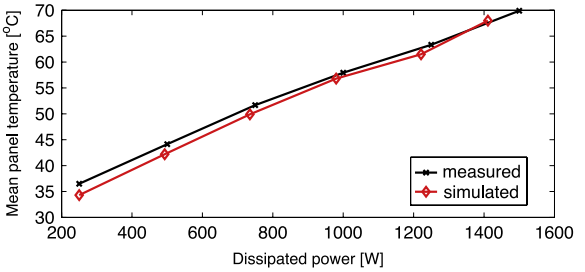

Fig. 19. Average panel temperature (computed vs. measured) as a function of the total dissipated power.

reliable operation of the device, since a re-wetting of the evaporator surface is mandatory. It is exactly this kind of optimization tasks for which the present mathematical model is beneficial, as it provides insight in the detailed performance and behavior of the cooling device.

Fig. 19 shows a plot of the mean temperature of the panel as a function of the dissipated power. While the computed temperature distribution describes in great detail the operation of the device, the mean panel temperature is a synthetic parameter for the designer to validate in an immediate manner the predictive capabilities of the code. Agreement of numerical results of Fig. 19 with experimental data is striking and indicates that, although based on many simplifying assumptions, our model does have very good predictive accuracy.

7. Conclusions and future work

In this article we have proposed and numerically implemented a multiscale thermo-fluid mathematical model for the description of a condenser component of a novel two-phase thermosiphon cooling system presented in [1,2]. The condenser consists of a set of roll-bonded vertically mounted fins among which air flows by either natural or forced convection and plays an important role in the industrial design of advanced power electronics systems.

The mathematical model is developed with the aim of deepening the understanding of the various thermo-fluid mechanisms that determine the performance of the condenser in view of a further optimization of the cooling device. The adopted approach is based on a multiscale formulation meant to reduce as much as possible the complexity required by a fully three-dimensional (3D) simulation code while maintaining reasonable predictive accuracy.

More specifically, the flow of the two-phase coolant within the condenser fins is modeled as a 1D network of pipes, while heat diffusion in the fins and its convective transport in the air slab are modeled as 2D processes. The resulting mathematical problem consists of a system of nonlinearly coupled PDEs in conservation form that are characterized by a mixed parabolic–hyperbolic character with possible presence of strongly advective dominating terms. A fixed point iterative map is used to reduce the computational effort to the successive solution of a sequence of decoupled linear stationary boundary value problems in the 1D channel pipe network and in the 2D air domain, respectively.

For the numerical approximation of the above differential problems a Primal Mixed Finite Element discretization method with upwind stabilization is used for the 1D coolant flow while a Dual Mixed-Finite Volume scheme with Exponential Fitting stabilization is used for 2D heat diffusion and convection.

Extensive numerical tests are carried out to validate the stability and accuracy of the proposed schemes on several benchmark problems whose solution is characterized by the presence of steep interior and boundary layers. The

obtained results confirm the good accuracy of the proposed formulation and its ability in satisfying a discrete maximum principle. This latter property confers robustness to the simulation tool and makes it suitable for heavy duty use in industrial applications.

The solver is then thoroughly applied to the numerical study and parametric characterization of a two-phase coolant system with realistic industrial geometry. The output of the simulations provides a complete map of the principal thermal and fluid dynamical variables of the problem (air temperature, coolant fluid pressure and vapor quality) that are extensively used by the project engineer to quantitatively design a novel device structure. Two groups of simulations are performed for the validation of the computational algorithm. In a first set of runs, the code is used to analyze the impact of channel geometry on the distribution of mass flow rate, vapor quality and panel temperature. In a second set of runs, the simulated average panel temperature of a given realistic cooler geometry is compared with available experimental data. Despite the several simplifying model assumptions introduced in the condenser mathematical description, the obtained results turn out to be in very good agreement with measures thus providing a sound indication of model reliability.

Even if applied to a problem arising in a specific area of thermo-fluid dynamical industrial applications, the multiscale modeling approach proposed in the present work can be used to study problems arising in other scientific contexts. For example, the computational model to couple 2D heat convection–diffusion and 1D flow in a pipeline network shares a close resemblance with the mathematical and numerical treatment of flow and mass transport in biological tissues that has been recently investigated in [36–38] and references cited therein. This interesting similarity might be profitably used to apply to these latter novel bio-technological applications solution methods that in this article are proved to enjoy properties of accuracy, stability and conservation.

Further research activity will be devoted to the:

- topological optimization of the channels layout;
- integration of the condenser model in a complete thermosiphon loop simulation tool including evaporator body and connections;
- analysis of the existence of a fixed point of the iterative map and its possible uniqueness.

Acknowledgments

The authors wish to express their gratitude to the anonymous referees for their valuable comments and remarks. RS was supported by the M.U.R.S.T. grant no. 200834WK7H005Adattività Numerica e di Modello per Problemi alle Derivate Parziali. CdF's work was partially funded by the Start-up Packages and Ph.D. Program project, co-funded by Regione Lombardia through the *Fondo per lo sviluppo e la coesione* 2007–2013, formerly FAS program.

Appendix. Dimensionality reduction of the heat convection–diffusion equations

In this section we illustrate the model reduction procedure that allows to derive under the assumptions (H1)–(H7) of Section 2.1 the simplified 2D model (1) from the corresponding 3-dimensional equations for heat convection and diffusion in the condenser walls and in the air between two plate walls. In order to describe the dimensionality reduction procedure, we start from the following model problem set in the 3D computational domain Ω depicted in Fig. A.20:

$$\begin{aligned}
&\nabla \cdot (-k\nabla u + \rho c \boldsymbol{v} u) = 0 && \text{in } \Omega \\
&u = u_{\text{in}} && \text{on } \Sigma_{\text{in}} \\
&-k\nabla u \cdot \boldsymbol{n} = 0 && \text{on } \Sigma_{\text{out}} \\
&(-k\nabla u + \rho c \boldsymbol{v} u) \cdot \boldsymbol{n} = h\,(u - u_w) && \text{on } \Sigma_w \\
&(-k\nabla u + \rho c \boldsymbol{v} u) \cdot \boldsymbol{n} = 0 && \text{on } \Sigma_{\text{lat}}.
\end{aligned} \tag{A.1}$$

We notice that the model problem (A.1) may describe either the forced heat convection between two fins or the heat diffusion in one fin wall. Referring to Fig. A.20, in the latter case, we have $\Sigma_{\text{in}} = \Sigma_{\text{out}} = \varnothing$, $\boldsymbol{v} = \boldsymbol{0}$ and $\Sigma_{\text{lat}} = \cup_{i=1}^{4} \Sigma_i$, while in the former case we have $\Sigma_{\text{in}} = \Sigma_1$, $\Sigma_{\text{out}} = \Sigma_3$ and $\Sigma_{\text{lat}} = \Sigma_2 \cup \Sigma_4$. The *contact walls* Σ_w, located at $z = 0$ and $z = S$ respectively, represent the boundaries where heat exchange occurs. According to assumption (H4), the

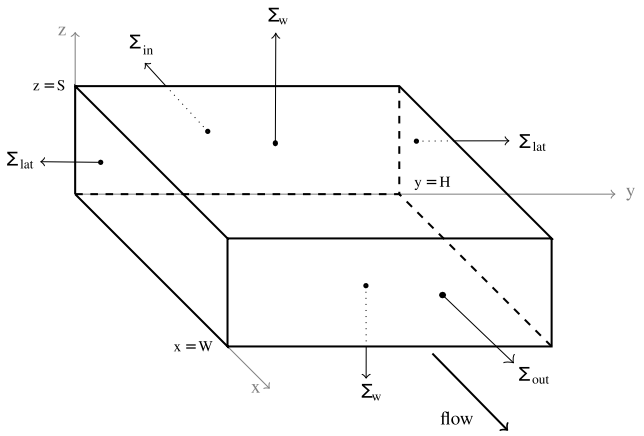

Fig. A.20. Three-dimensional domain for the heat convection–diffusion model problem.

convection velocity $\boldsymbol{v}$ is directed along the x axis, so that it can be expressed as

$$\boldsymbol{v}(z) = \boldsymbol{V}\, B(z) \tag{A.2}$$

where $\boldsymbol{V}$ is a constant vector directed along the x axis and $B(z)$ is a dimensionless scalar shape function accounting for the velocity boundary layer in the z direction.

The unknown function $u = u(x, y, z)$ represents a temperature (either air temperature or wall temperature), ρ is the density of the medium contained in the domain Ω, c is the specific heat capacity of the medium and k is its thermal conductivity.

Temperature is fixed at the inlet surface Σ_{in} to a given value u_{in}. On the contact surfaces Σ_w the outflow heat flux is proportional to the difference between temperature u and the wall temperature u_w, through the *heat transfer coefficient* h. $\boldsymbol{n}$ is the outward unit vector along the external surface of the domain.

According to assumptions (H1) and (H3), the conditions at the upper and the lower contact surface Σ_w are symmetric. Therefore, we can define an adiabatic plane at $z = S/2$ which allows us to consider only the portion of space between the adiabatic surface and one of the two contacts Σ_w, for example that located at $z = 0$.

We start our dimensionality reduction procedure by assuming the following ansatz for the unknown u

$$u(x, y, z) = U(x, y)\, Z(z), \tag{A.3}$$

where $U = U(x, y)$ expresses temperature variation in the xy plane, while $Z = Z(z)$ is a dimensionless shape function accounting for temperature variation between the contact surface and the adiabatic plane located at $z = S/2$. The separated variable form of temperature distribution (A.3) agrees well with assumptions (H6) and (H7) according to which a mild variation of temperature between two neighboring contact surfaces is to be expected. The next step consists in examining the dependence of problem coefficients on the unknown u. The heat capacity c can be taken as a constant [39]. The same holds for the density ρ (cf. assumption (H5)). As far as the thermal conductivity k, the following power law can be used [39]

$$k(x, y, z) = k_0 \left(\frac{u(x, y, z)}{u_0} \right)^{\beta} = k_0 \left(\frac{U(x, y) Z(z)}{u_0} \right)^{\beta} \tag{A.4}$$

where k_0, u_0 and β are suitable constants.

Integration of the balance equation in the vertical direction and the use of (A.2)–(A.4) yield

$$\lambda_1 \nabla_{xy} \cdot \left(-k_0 \left(\frac{U}{u_0} \right)^{\beta} \nabla_{xy} U \right) + \lambda_2 \nabla_{xy} \cdot (\rho c \boldsymbol{V} U) + \mathbb{I} = 0 \tag{A.5}$$

where

$$\lambda_1 := \int_0^{S/2} Z^{\beta+1}(z)\, dz, \qquad \lambda_2 := \int_0^{S/2} Z(z)\, B(z)\, dz \tag{A.6}$$

and

$$\mathbb{I} := \int_0^{S/2} \partial_z \left(-k\partial_z u\right) dz,$$

while $\boldsymbol{\nabla}_{xy}(\cdot)$ is the gradient operator with respect to the directions x and y only, The quantity λ_1 modulates the variation of thermal conductivity in the z direction while the quantity λ_2 is related to the shape of the thermal boundary layer arising at the interface between air and panel. Using Gauss theorem to treat the quantity $\mathbb{I}$ we get

$$\mathbb{I} = \left[-k\partial_z u\right]_0^{S/2} = -\left(-k\partial_z u|_{z=0}\right)$$

because $-k\partial_z u|_{z=S/2} = 0$ under the assumption of adiabatic surface, so that we can rewrite condition (A.1)$_4$ as

$$h\left(u|_{z=0} - u_w\right) = \left(-k\boldsymbol{\nabla} u + \rho c u \boldsymbol{v}\right)\cdot \boldsymbol{n}|_{\Sigma_w} = -k\boldsymbol{\nabla} u \cdot \boldsymbol{n}|_{\Sigma_w} = -\left(-k\partial_z u|_{z=0}\right) = \mathbb{I}.$$

Therefore, upon rescaling the shape function Z in such a way that $Z(0) = 1$, Eq. (A.5) becomes

$$\lambda_1 \boldsymbol{\nabla}_{xy}\cdot\left(-k_{xy}\boldsymbol{\nabla}_{xy}U\right) + \lambda_2 \boldsymbol{\nabla}_{xy}\cdot\left(\rho c \boldsymbol{V} U\right) + h\left(U - u_w\right) = 0$$

where we have defined the heat conductivity in the xy plane (contact surface)

$$k_{xy} := k_0\left(\frac{U(x,y)}{u_0}\right)^{\beta} = k_0\left(\frac{U(x,y)Z(0)}{u_0}\right)^{\beta} = k(x,y,0).$$

To end up with a 2D reduced model for heat convection and diffusion, we need specify the exponent β. At low pressures we typically have $\beta = 0.9$ [39] so that k is approximately a linear function of temperature. This latter quantity is used as a fitting parameter in the numerical simulations reported in Section 6. Thus, omitting the subscript xy in the notation, and writing u instead of U, the reduced 2D version of (A.1) reads:

$$\begin{cases} \boldsymbol{\nabla}\cdot\left(-k\boldsymbol{\nabla} u + \rho c\widehat{\boldsymbol{v}} u\right) + \widehat{h}(u - u_w) = 0 & (x,y)\in\Omega, \\ u = u_{\text{in}} & x = 0, \\ -k\boldsymbol{\nabla} u\cdot\boldsymbol{n} = 0 & x = W, \\ \left(-k\boldsymbol{\nabla} u + \rho c\widehat{\boldsymbol{v}} u\right)\cdot\boldsymbol{n} = 0 & y = 0,\ y = H, \end{cases} \tag{A.7}$$

where $\Omega := (0,W)\times(0,H)$, $\widehat{h} := h/\lambda_1$, $\widehat{\lambda} := \lambda_2/\lambda_1$ and $\widehat{\boldsymbol{v}} := \widehat{\lambda}\boldsymbol{V}$. Notice that the two heat balance equations (1a) and (1b) are special instances of (A.7) upon setting $u = T_a, k = k_a, \rho = \rho_a, c = c_p, \widehat{\boldsymbol{v}} = \widetilde{\boldsymbol{v}}_a, \widehat{h} = \widetilde{h}_{aw}$ and $u_w = T_w$ in the case of the air temperature model, and $u = T_w, k = k_w, \widehat{\boldsymbol{v}} = \boldsymbol{0}, \widehat{h} = h^*_{aw} + h^*_{wc}$, and $u_w = (h^*_{aw}T_a + h^*_{wc}T_c)/(h^*_{aw} + h^*_{wc})$ in the case of the panel temperature model, respectively.

References

[1] F. Agostini, T. Gradinger, Roll-bond condenser in a two-phase thermosyphon loop for power electronics cooling, in: D. Poljak, B. Sunden, C.A. Brebbia (Eds.), Advanced Computational Methods and Experiments in Heat Transfer XII, in: Transactions of the Wessex Institute collection, vol. 75, The Wessex Institute, 2012.

[2] F. Agostini, T. Gradinger, C. de Falco, Simulation aided design of a two-phase thermosyphon for power electronics cooling, in: IECON 2011-37th Annual Conference on IEEE Industrial Electronics Society, IEEE, 2011, pp. 1560–1565.

[3] C. Lasance, Technical data column, in: Electronics Cooling, 1997.

[4] A. Bar-Cohen, W.M. Rohsenow, Thermally optimum spacing of vertical, natural convection cooled, parallel plates, J. Heat Transfer 106 (1984) 116.

[5] F.P. Incropera, D.P. De Witt, Fundamentals of Heat and Mass Transfer, John Wiley and Sons Inc., New York, NY, 2002.

[6] Christopher E. Brennen, Fundamentals of Multiphase Flow, Cambridge University Press, 2005.

[7] S. Levy, Two-Phase Flow in Complex Systems, John Wiley & Sons, 1999.

[8] C.J.L. Hermes, C. Melo, C.O.R. Negrao, A numerical simulation model for plate-type, roll-bond evaporators, Int. J. Refrig. 31 (2) (2008) 335–347.

[9] M.K. Banda, M. Herty, A. Klar, Gas flow in pipeline networks, Netw. Heterog. Media 1 (1) (2006).

[10] J. Brouwer, I. Gasser, M. Herty, Gas pipeline models revisited: Model hierarchies, nonisothermal models, and simulations of networks, Multiscale Model. Simul. 9 (2) (2011) 601–623.

[11] M. Herty, Coupling conditions for networked systems of Euler equations, SIAM J. Sci. Comput. 30 (3) (2008) 1596–1612.

[12] L. Formaggia, A. Fumagalli, A. Scotti, P. Ruffo, A reduced model for Darcy's problem in networks of fractures, Technical Report MOX-Report No. 32/2012, MOX, Dipartimento di Matematica, Politecnico di Milano, P.zza L. da Vinci 32—20133 Milano, Italy, 2012.

[13] E.W. Lemmon, R. Span, Short fundamental equations of state for 20 industrial fluids, J. Chem. Eng. Data 51 (3) (2006) 785–850.
[14] R. Tillner-Roth, H.D. Baehr, An international standard formulation for the thermodynamic properties of 1,1,1,2-tetrafluoroethane (hfc-134a) for temperatures from 170 K to 455 K and pressures up to 70 MPa, J. Phys. Chem. Ref. Data 23 (5) (1994) 657–729.
[15] E.W. Lemmon, M.L. Huber, M.O. McLinden, Nist standard reference database 23: Reference fluid thermodynamic and transport properties-refprop, version 9.1. National Institute of Standards and Technology, Standard Reference Data Program, 2013.
[16] A. Cavallini, G. Censi, D. Del Col, L. Doretti, G.A. Longo, L. Rossetto, C. Zilio, Condensation inside and outside smooth and enhanced tubes—a review of recent research, Int. J. Refrig. 26 (4) (2003) 373–392.
[17] O. Garcia-Valladares, Review of in-tube condensation heat transfer correlations for smooth and microfin tubes, Heat Transfer Eng. 24 (4) (2003) 6–24.
[18] M.M. Shah, A general correlation for heat transfer during film condensation inside pipes, Int. J. Heat Mass Transfer 22 (4) (1979) 547–556.
[19] L. Carichino, Computational models for power electronics cooling systems, (Master's Thesis) Politecnico di Milano, 2010.
[20] J.R. Thome, Engineering Data Book III, Wolverine Tube, Inc., 2006.
[21] F. Brezzi, M. Fortin, Mixed and Hybrid Finite Element Methods, Springer Verlag, New York, 1991.
[22] Martin Vohralík, Equivalence between mixed finite element and multi-point finite volume methods, C. R. Math. 339 (7) (2004) 525–528.
[23] J. Douglas Jr., J.E. Roberts, Global estimates for mixed method for second order elliptic equations, Math. Comp. 44 (169) (1985) 39–52.
[24] T. Arbogast, Z. Chen, On the implementation of mixed methods as nonconforming methods for second-order elliptic problems, Math. Comp. 64 (211) (1995) 943–972.
[25] R. Sacco, F. Saleri, Stabilized mixed finite volume methods for convection–diffusion problems, East-West J. Numer. Math. 5 (4) (1997) 291–311.
[26] F. Brezzi, L.D. Marini, S. Micheletti, P. Pietra, R. Sacco, Stability and error analysis of mixed finite volume methods for advective–diffusive problems, Comput. Math. Appl. 51 (2006) 681–696.
[27] P.A. Raviart, J.M. Thomas, A mixed finite element method for second order elliptic problems, in: I. Galligani, E. Magenes (Eds.), Mathematical Aspects of Finite Element Methods, I, Springer-Verlag, Berlin, 1977.
[28] L.D. Marini, P. Pietra, An abstract theory for mixed approximations of second order elliptic problems, Mat. Appl. Comput. 8 (1989) 219–239.
[29] R.R.P. van Nooyen, A Petrov–Galerkin mixed finite element method with exponential fitting, Numer. Methods Partial Differential Equations 11 (5) (1995) 501–524.
[30] M. Farhloul, M. Fortin, A mixed finite element for the Stokes problem using quadrilateral elements, Adv. Comput. Math. 3 (1995) 101–113.
[31] R.S. Varga, Matrix Iterative Analysis, Englewood Cliffs, New Jersey, 1962.
[32] D.L. Scharfetter, H.K. Gummel, Large signal analysis of a silicon read diode oscillator, IEEE Trans. Electron Devices ED-16 (1969) 64–77.
[33] H.G. Roos, M. Stynes, L. Tobiska, Numerical Methods for Singularly Perturbed Differential Equations, Springer-Verlag, Berlin, Heidelberg, 1996.
[34] J. Xu, L. Zikatanov, A monotone finite element scheme for convection–diffusion equations, Math. Comp. 68 (228) (1999) 1429–1446.
[35] J.E. Roberts, J.M. Thomas, Mixed and hybrid methods, in: P.G. Ciarlet, J.L. Lions (Eds.), Finite Element Methods, Part I, Vol. 2, North-Holland, Amsterdam, 1991.
[36] C. d'Angelo, Multiscale modelling of metabolism and transport phenomena in living tissues, (Ph.D. Dissertation) EPFL, 2007.
[37] R.J. Shipley, S.J. Chapman, Multiscale modelling of fluid and drug transport in vascular tumours, Bull. Math. Biol. 72 (6) (2010) 1464–1491.
[38] K. Erbertseder, J. Reichold, B. Flemisch, P. Jenny, R. Helmig, A coupled discrete/continuum model for describing cancer-therapeutic transport in the lung, PLoS One 7 (3) (2012) e31966.
[39] A.A. Wasserman, Ya.Z. Kazavchinskiy, V.A. Rabinovich, Thermophysical Properties of Air and its Components, Science, Moscow, 1966.